Inorganic Chemistry
Article
pubs.acs.org/IC

Platinum Chloride Complexes Containing 6-[9,9-Di(2-ethylhexyl)-7-R-9*H*-fluoren-2-yl]-2,2′-bipyridine Ligand (R = NO_2, CHO, Benzothiazol-2-yl, *n*-Bu, Carbazol-9-yl, NPh_2): Tunable Photophysics and Reverse Saturable Absorption

Zhongjing Li, Ekaterina Badaeva, Angel Ugrinov, Svetlana Kilina, and Wenfang Sun*

Department of Chemistry and Biochemistry, North Dakota State University, Fargo, North Dakota 58108-6050, United States

Supporting Information

ABSTRACT: Six new platinum(II) chloride complexes **1−6** containing a 6-[9,9-di(2-ethylhexyl)-7-R-9*H*-fluoren-2-yl]-2,2′-bipyridine (R = NO_2, CHO, benzothiazol-2-yl (BTZ), *n*-Bu, carbazol-9-yl (CBZ), NPh_2) ligand were synthesized and characterized. The influence of the electron-donating or electron-withdrawing substituent at the 7-position of the fluorenyl component on the photophysics of these complexes was systematically investigated by spectroscopic methods and simulated by time-dependent density functional theory (TDDFT). Electron-withdrawing or -donating substituents exert distinct effects on the photophysics of the complexes. All complexes feature a low-energy, broad ^{1}MLCT (metal-to-ligand charge transfer)/^{1}ILCT (intraligand charge transfer)/$^1\pi,\pi^*$ absorption band (tail) above ca. 430 nm and a major absorption band(s) between 320 and 430 nm, which admix ^{1}MLCT, $^1\pi,\pi^*$, ^{1}ILCT, and/or ^{1}LLCT (ligand-to-ligand charge transfer) characters. The contributions of different configurations to the major absorption band(s) vary depending on the nature of the substituent. Strong electron-donating or -withdrawing substituents (NPh_2 and NO_2) and the aromatic substituent BTZ cause a pronounced red-shift of the absorption spectra of **1**, **3**, and **6**. All complexes are emissive at room temperature and at 77 K. The emitting excited state is dominated by $^3\pi,\pi^*$ character in **1−3**, with some contributions from ^{3}MLCT in **1** and **2**, while the emission is predominantly from the ^{3}MLCT state for **4** and **5** but with some $^3\pi,\pi^*$ character. For **6**, the emitting state is ^{3}ILCT in nature. With the increased electron-donating ability of the substituent, the $^3\pi,\pi^*$ character diminishes while charge transfer character increases. All complexes exhibit broad and strong triplet excited-state absorption (TA) from the near-UV to the near-IR spectral region. The TA band maxima are red-shifted for complexes **1−3** (which possess the electron-withdrawing substituents) compared to those of **4−6** (which contain electron-donating substituents). All complexes manifest strong reverse saturable absorption (RSA) for a nanosecond laser pulse at 532 nm, which originates from the much stronger triplet excited-state absorption than the ground-state absorption of **1−6** in the visible spectral region. The strength of RSA follows this trend: **4** ≈ **5** < **1** ≈ **3** < **2** < **6**, which is primarily determined by the ratio of the triplet excited-state absorption cross section relative to that of the ground-state absorption (σ_{ex}/σ_0) at 532 nm. The σ_{ex}/σ_0 ratios (116−261) of **1−6** at 532 nm are much larger than those of most of the reverse saturable absorbers reported in the literature, with the ratio of **6** (σ_{ex}/σ_0 = 261) being among the largest values reported to date. This makes complexes **1−6**, especially **6**, very promising reverse saturable absorbers.

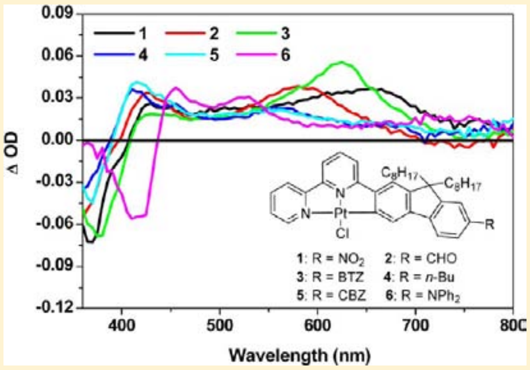

INTRODUCTION

Platinum(II) complexes have been fascinating for decades due to their rich photophysics and potential applications in various photonic devices and in cancer treatment.[1] For instance, Lippard's group has extensively investigated the application of platinum complexes as anticancer reagents;[2] Che and coworkers employed platinum(II) diimine arylacetylide complexes and cyclometalated 6-aryl-2,2′-bipyridine arylacetylide platinum complexes in organic light emitting devices;[3] The Eisenberg,[4] Schanze,[5] and Yam[6] groups independently studied the application of platinum complexes in dye sensitized solar cells; our group and several other groups reported the utilization of platinum complexes as chemical sensors.[7] In recent years, our group and Schanze's group have also extensively explored the application of various Pt(II) complexes as nonlinear transmission materials.[8]

Compared to bidentate ligands, terdentate ligands are more resistant to distortion toward D_{2d} conformations when coordinated with d^8 transition metals, and thus disfavor nonradiative processes.[9] Terpyridine ligands stand out for their preference to adopt planar geometries. Unfortunately, the binding angle of terpyridine is not ideal when forming a square planar configuration,[10] which reduces the ligand field and thus

Received: March 20, 2013
Published: June 17, 2013

Scheme 1. Synthetic Scheme and Structures for Complexes 1−6 (C_8H_{17} = 2-Ethylhexyl)

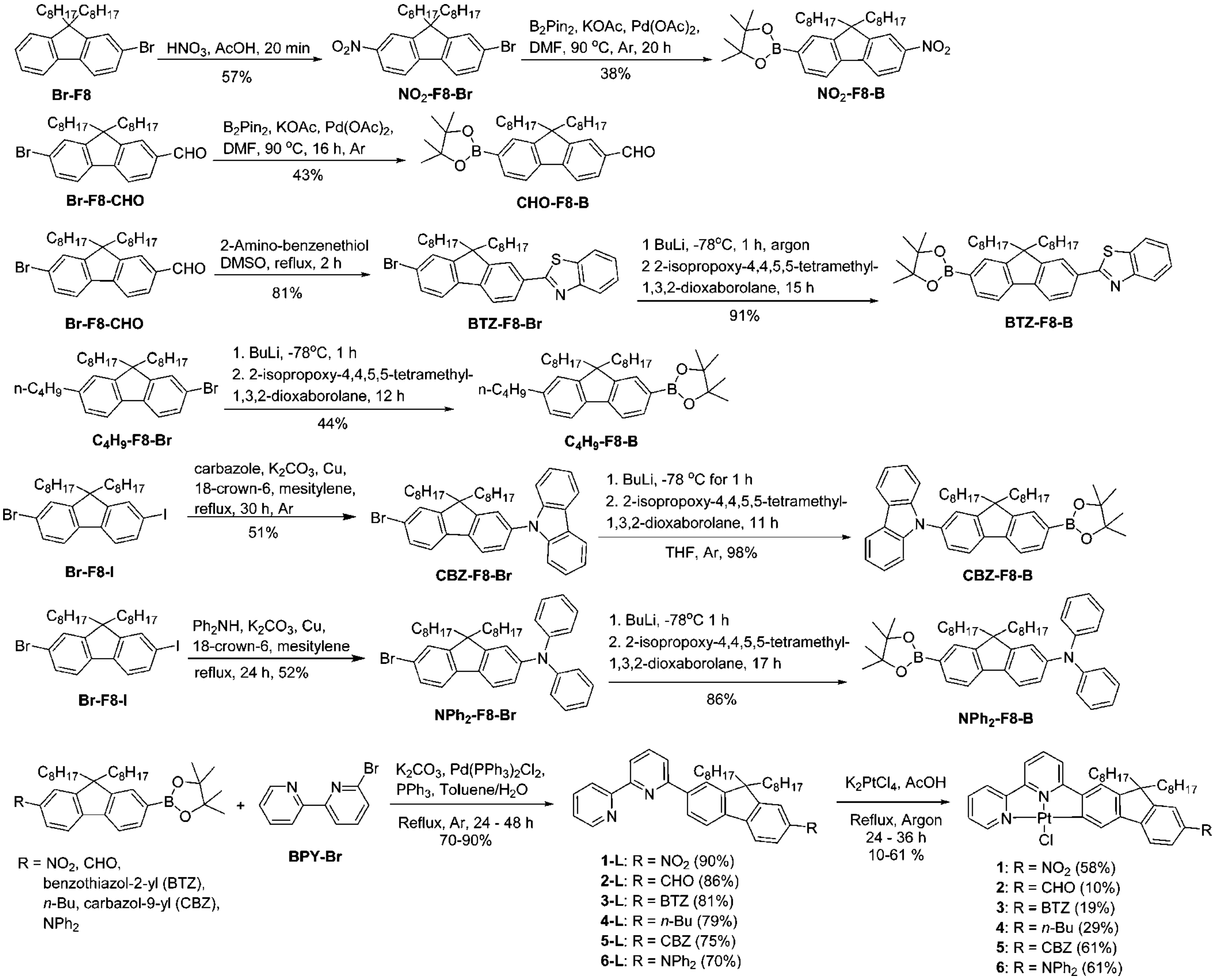

facilitates the accessibility of the deactivating metal-centered d−d state. In contrast, terdentate cyclometalating ligands with a C^N^N framework, by incorporating an hydrocarbon aryl unit at the 6-position of 2,2′-bipyridine, have shown several merits over terpyridine ligands. First, cyclometalation makes it possible to construct a neutral inner coordination sphere. Second, the strong σ donating ability of the ligating C^- atom and good π accepting capability of the bipyridine motif offer the metal center a strong ligand field, which increases the d−d excited state and consequently reduces the deactivation of the lowest-energy charge transfer excited state via the d−d excited state. Third, the C^N^N type ligand would form a less-distorted square-planar geometry with the d^8 transition metals, which reduces the radiationless decay as well. Fourth, the stronger π-donating ability of the 6-aryl ring could also introduce some intraligand charge transfer character into the lowest excited states, resulting in a long-lived triplet excited state.

In one of our previous studies, we found that incorporation of fluorenyl substituent to the 4-position of the center pyridine ring of the terpyridine ligand could efficiently increase the emission efficiency, prolong the triplet excited-state lifetime, and increase the ratio of the excited-state absorption cross section relative to the ground-state absorption cross section in Pt(II) complexes.[8c] As a result, stronger reverse saturable absorption was obtained. Inspired by this investigation and by the merit of C^N^N ligand vs terpyridine ligand, we recently designed a complex with the C^N^N framework that incorporates fluorene at the 6-position of the bipyridine.[11] The complex features large ratios of excited-state absorption cross section to ground-state absorption cross section in the visible spectral region and strong two-photon absorption in the near-IR region. Both of them account for the strong nonlinear transmission of the complex. These results are quite exciting; however, the structure−property correlations in Pt(II) complexes with this type of C^N^N ligand have not been explored yet. In addition, in order to further improve the reverse saturable absorption of this type of Pt(II) complexes, it is critical to reduce the ground-state absorption of the complexes in the visible spectral region. This could be realized by replacing the 4-tolylacetylide coligand by chloride coligand, which would reduce the contribution of the ligand-to-ligand charge transfer (LLCT) to the lowest excited state and cause hyposochromic shift of the charge transfer absorption band. Taking these factors into account, we designed and synthesized six new Pt(II) complexes (structures of the new complexes **1**−**6** are illustrated in Scheme 1) with different electron-donating or

-withdrawing substituents at the 7-position of the fluorene component. In order to increase the solubility of the Pt(II) complexes, branched alkyl chains (2-ethylhexyl) were introduced at the 9-positon of the fluorene. Here we report the synthesis, photophysics, and reverse saturable absorption of these complexes. Insights into the nature of optical transitions have also been obtained from the time-dependent density functional theory (TDDFT) calculations.

■ EXPERIMENTAL SECTION

Synthesis and Characterization. The synthetic routes for **1**−**6** are illustrated in Scheme 1. All of the reagents and solvents were purchased from Aldrich Chemical Co. or Alfa Aesar and used as is unless otherwise stated. Silica gel for column chromatography was purchased from Sorbent Technology (60 Å, 230−400 mesh, 500−600 m^2/g, pH: 6.5−7.5). The synthesis of precursors **Br-F8-I**,[12] **Br-F8-CHO**,[13] **CHO-F8-B**,[14] **Br-F8**,[15] **NO$_2$-F8-Br**,[16] **NO$_2$-F8-B**,[16] **BTZ-F8-Br**,[17] **CBZ-F8-B**,[18] **NPh$_2$-F8-B**,[8d] **C$_4$H$_9$-F8-B**,[19] and **BPY-Br**[20] followed the literature procedures. **BTZ-F8-B** was obtained by reacting **BTZ-F8-Br** in THF solution at −78 °C with 1 equiv of BuLi followed by addition of 1 equiv of 2-isopropoxy-4,4,5,5-tetramethyl-1,3,2-dioxaborolane. All intermediates were characterized by ^{1}H NMR. The synthetic details and ^{1}H NMR data of these intermediates are provided in the Supporting Information. The general procedures for the synthesis of ligands **1-L**−**6-L** and for complexes **1**−**6** are provided below. Ligands **1-L**−**6-L** and complexes **1**−**6** were all characterized by ^{1}H NMR, electrospray ionization high-resolution mass spectrometry (ESI-HRMS), and elemental analyses.

Table 1. Single Crystal X-ray Parameters and Refinement Data for 1

T (K)	100(2)
λ (Å)	0.71073
formula	$C_{39}H_{46}ClN_3O_2Pt\cdot CH_2Cl_2$
MW	904.25
crystal size (mm)	0.33 × 0.12 × 0.09
crystal system	monoclinic
space group	$P2(1)/n$
a (Å)	12.7116(9)
b (Å)	17.5310(11)
c (Å)	17.1311(11)
α (deg)	90
β (deg)	90.489(1)
γ (deg)	90
V (Å^3)	3817.5(4)
Z	4
ρ_{calc} (g/cm^3)	1.573
μ (cm^{-1})	3.924
radiation type	Mo
F(000)	1816
reflns collected	65292
unique reflns	11451
no. of reflns ($I \geq 2\sigma$)	8722
resolution (Å)	0.7
gof on F^2	1.022
R_1/wR_2 ($I \geq 2\sigma(I)$)[a]	0.0317/0.0732
R_1/wR_2 (all data)[a]	0.0529/0.0827

[a] $R_1 = \sum||F_o| - |F_c||/\sum|F_o|$, $wR_2 = [\sum(w(F_o^2 - F_c^2)^2)/\sum w(F_o^2)^2]^{1/2}$ for $F_o^2 > 2\sigma(F_o^2)$, $w = 1/[\sigma^2(F_o^2) + (AP)^2 + BP]$, where $P = (F_o^2 + 2F_c^2)/3$; A (B) = 0.0370 (5.4894).

^{1}H NMR spectra were obtained on Varian Oxford-VNMR spectrometers (300 MHz, 400 MHz, or 500 MHz). ESI-HRMS analyses were performed on a Bruker BioTOF III mass spectrometer. Elemental analyses were conducted by NuMega Resonance Laboratories, Inc. in San Diego, California.

General Procedure for the Synthesis of Ligands 1-L−6-L. The mixture of **R-F8-B** (1 mmol), 6-bromo-2,2′-bipyridine (235 mg, 1 mmol), K_2CO_3 (410 mg, 3 mmol), $Pd(PPh_3)_2Cl_2$ (30 mg), and PPh_3 (60 mg) in toluene (20 mL) and water (10 mL) was heated to reflux under argon for 40 h. After reaction, the organic layer was collected, washed with brine (30 mL × 3), and dried over $MgSO_4$. Then the solvent was removed to obtain the crude product. The crude product was purified using column chromatography.

1-L. Purified by silica gel column chromatography eluting with dichloromethane. 0.53 g of pale yellow solid was obtained (yield: 90%). ^{1}H NMR ($CDCl_3$, 400 MHz): 8.70−8.71 (m, 1H), 8.63−8.65 (m, 1H), 8.40−8.42 (m, 1H), 8.27−8.29 (m, 2H), 8.19−8.22 (m, 2H), 7.80−7.94 (m, 5H), 7.32−7.35 (m, 1H), 2.08−2.18 (m, 4H), 0.48−0.83 (m, 30H). ESI-HRMS: m/z calc for $[C_{39}H_{47}N_3O_2 + H]^+$: 590.3741. Found: 590.3734. Anal. Calc for $C_{39}H_{47}N_3O_2$: C, 79.42; H, 8.03; N, 7.12. Found: C, 79.13; H, 8.06; N, 7.15.

2-L. Purified by silica gel column chromatography eluting with dichloromethane. 0.49 g of yellow oil was obtained (yield: 86%). ^{1}H NMR ($CDCl_3$, 400 MHz): 10.07 (s, 1H), 8.69−8.70 (m, 1H), 8.64−8.66 (m, 1H), 8.40 (d, J = 8.0 Hz, 1H), 8.16−8.21 (m, 2H), 7.94−7.97 (m, 1H), 7.80−7.92 (m, 6H), 7.31−7.34 (m, 1H), 2.06−2.19 (m, 4H), 0.46−0.86 (m, 30H). ESI-HRMS: m/z calc for $[C_{40}H_{48}N_2O + H]^+$: 573.3839. Found: 573.3823. Anal. Calc for $C_{40}H_{48}N_2O$: C, 83.87; H, 8.45; N, 4.89. Found: C, 83.49; H, 8.80; N, 4.82.

3-L. Purified by silica gel column chromatography eluting with hexane/ethyl acetate (10:1 v/v). 0.55 g of yellow oil was obtained (yield: 81%). ^{1}H NMR ($CDCl_3$, 400 MHz): 8.64−8.70 (m, 2H), 8.36−8.39 (m, 1H), 8.07−8.19 (m, 5H), 7.80−7.91 (m, 6H), 7.46−7.50 (m, 1H), 7.30−7.38 (m, 2H), 2.15−2.17 (m, 4H), 0.48−0.95 (m, 30H). ESI-HRMS: m/z calc for $[C_{46}H_{51}N_3S + H]^+$: 678.3876. Found: 678.3884. Anal. Calc for $C_{46}H_{51}N_3S\cdot 0.33DMF\cdot 0.33CH_2Cl_2$: C, 77.81; H, 7.45; N, 6.39. Found: C, 77.51; H, 7.50; N, 6.46.

4-L. Purified by silica gel column chromatography eluting first with hexane/dichloromethane (2:1 v/v) and then with hexane/ethyl acetate (5:1 v/v). 0.47 g of yellow oil was obtained (yield: 79%). ^{1}H NMR ($CDCl_3$, 400 MHz): 8.65−8.69 (m, 2H), 8.35 (dd, J = 7.6, 0.8 Hz, 1H), 8.08−8.13 (m, 2H), 7.73−7.88 (m, 4H), 7.62 (d, J = 7.6 Hz, 1H), 7.28−7.32 (m, 1H), 7.20 (s, 1H), 7.13 (dd, J = 7.8, 1.4 Hz, 1H), 2.67 (t, J = 7.6 Hz, 2H), 1.96−2.12 (m, 4H), 1.59−1.64 (m, 2H), 1.31−1.39 (m, 2H), 0.47−0.96 (m, 33H). ESI-HRMS: m/z calc for $[C_{43}H_{56}N_2 + H]^+$: 601.4516. Found: 601.4514. Anal. Calc for $C_{43}H_{56}N_2\cdot 0.67$toluene: C, 86.44; H, 9.33; N, 4.23. Found: C, 86.80; H, 9.70; N, 4.60.

5-L. Purified by silica gel column chromatography eluting with dichloromethane. 0.78 g of yellow oil was collected as the product (yield: 75%). ^{1}H NMR ($CDCl_3$, 400 MHz): 8.68−8.72 (m, 2H), 8.40 (d, J = 7.6 Hz, 1H), 8.16−8.24 (m, 4H), 7.97 (d, J = 7.6 Hz, 1H), 7.83−7.94 (m, 4H), 7.51−7.61 (m, 2H), 7.28−7.43 (m, 7H), 1.98−2.25 (m, 4H), 0.52−0.98 (m, 30H). ESI-HRMS: m/z calc for $[C_{51}H_{55}N_3 + H]^+$: 710.4469. Found: 710.4475. Anal. Calc for $C_{51}H_{55}N_3\cdot 0.17CH_2Cl_2$: C, 84.86; H, 7.70; N, 5.80. Found: C, 85.08; H, 7.98; N, 5.74.

6-L. Purified by silica gel column chromatography eluting with dichloromethane. 0.50 g of yellow oil was obtained (yield: 70%). ^{1}H NMR ($CDCl_3$, 400 MHz): 8.64−8.69 (m, 2H), 8.34 (d, J = 7.6 Hz, 1H), 8.12 (dd, J = 8.2, 1.4 Hz, 1H), 8.06 (m, 1H), 7.83−7.89 (m, 2H), 7.78 (d, J = 7.6 Hz, 1H), 7.71 (m, 1H), 7.60−7.63 (m, 1H), 7.29−7.33 (m, 1H), 7.19−7.24 (m, 4H), 7.05−7.13 (m, 6H), 6.67−7.01 (m, 2H), 1.84−2.08 (m, 4H), 0.51−1.02 (m, 30H). ESI-HRMS: m/z calc for $[C_{51}H_{57}N_3 + H]^+$: 712.4625. Found: 712.4623. Anal. Calc for $C_{51}H_{57}N_3$: C, 86.03; H, 8.07; N, 5.90. Found: C, 86.29; H, 8.20; N, 5.71.

General Procedure for the Synthesis of Complexes 1−6. The mixture of ligand (0.5 mmol), K_2PtCl_4 (0.5 mmol), and acetic acid (10 mL) was heated to reflux under argon for 24 h. After reaction, the solvent was removed. The red residual was dissolved in dichloromethane, washed with brine (10 mL × 3), and dried over $MgSO_4$. Purification was carried out by running flash silica gel column

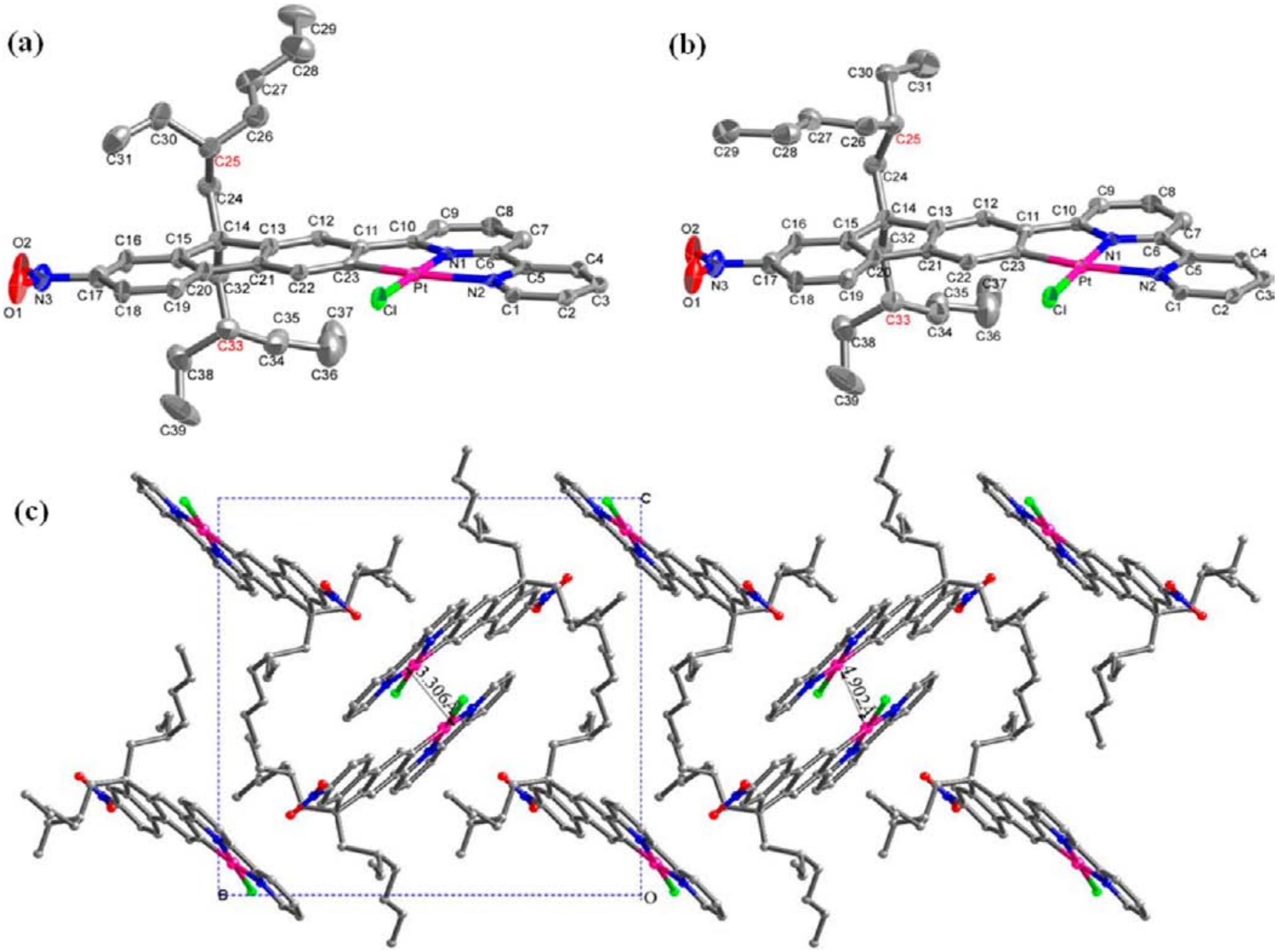

Figure 1. (a) Structure of the diastereomer in which C25's configuration is *R*; the percentage of this diastereomer is 52%. (b) Structure of the diastereomer in which C25's configuration is *S*; the percentage of this diastereomer is 48%. (c) 3D packing of complex **1** viewed along the *a* axis.

chromatography eluting with dichloromethane, and then recrystallization from dichloromethane and hexane.

1. 237 mg of orange powder was obtained (yield: 58%). ^{1}H NMR ($CDCl_3$, 400 MHz): 9.15−9.19 (m, 1H), 8.21−8.29 (m, 3H), 8.03−8.08 (m, 1H), 7.85−7.95 (m, 3H), 7.58−7.67 (m, 3H), 7.38 (m, 1H), 1.98−2.08 (m, 4H), 0.44−0.93 (m, 30H). ESI-HRMS: *m*/*z* calc for $[C_{39}H_{46}N_3O_2ClPt + H]^+$: 820.3001. Found: 820.3003. Anal. Calc for $C_{39}H_{46}N_3O_2ClPt$: C, 57.17; H, 5.66; N, 5.13. Found: C, 56.98; H, 5.68; N, 5.11.

2. 40 mg of red powder was obtained (yield: 10%). ^{1}H NMR ($CDCl_3$, 400 MHz): 10.05 (s, 1H), 8.88−8.93 (m, 1H), 8.12−8.23 (m, 1H), 7.84−7.92 (m, 5H), 7.73−7.79 (m, 1H), 7.56 (d, *J* = 8.0 Hz, 1H), 7.43−7.50 (m, 2H), 7.33 (d, *J* = 2.8 Hz, 1H), 1.96−2.09 (m, 4H), 0.42−0.93 (m, 30H). ESI-HRMS: *m*/*z* calc for $[C_{40}H_{47}N_2ClOPt + H]^+$: 803.3100. Found: 803.3072. Anal. Calc for $C_{40}H_{47}ClN_2OPt$: C, 59.88; H, 5.90; N, 3.49. Found: C, 59.88; H, 6.28; N, 3.37.

3. 86 mg of yellow powder was obtained (yield: 19%). ^{1}H NMR ($CDCl_3$, 400 MHz): 9.14−9.17 (m, 1H), 8.18 (s, 1H), 8.01−8.11 (m, 4H), 7.88−7.94 (m, 3H), 7.80−7.85 (m, 1H), 7.60−7.64 (m, 1H), 7.53−7.57 (t, *J* = 7.8 Hz, 2H), 7.45−7.49 (m, 1H), 7.33−7.37 (m, 2H), 1.98−2.13 (m, 4H), 0.45−0.93 (m, 30H). ESI-HRMS: *m*/*z* calc for $[C_{46}H_{50}N_3ClSPt + H]^+$: 908.3137. Found: 908.3132. Anal. Calc for $C_{46}H_{50}ClN_3PtS$: C, 60.88; H, 5.55; N, 4.63; S, 3.53. Found: C, 60.73; H, 5.90; N, 4.47; S, 3.92.

4. 120 mg of orange powder was obtained (yield: 29%). ^{1}H NMR ($CDCl_3$, 500 MHz): 8.80 (dd, *J* = 22, 5.3 Hz, 1H), 8.03−8.10 (m, 1H), 7.83−7.92 (m, 2H), 7.66−7.73 (m, 2H), 7.50−7.53 (m, 1H), 7.36−7.45 (m, 2H), 7.25−7.30 (m, 1H), 7.17 (s, 1H), 7.13−7.15 (m, 1H), 2.68 (t, *J* = 7.5 Hz, 2H), 1.93−2.03 (m, 4H), 1.60−1.67 (m, 2H), 1.32−1.42 (m, 2H), 0.48−1.00 (m, 33H). ESI-HRMS: *m*/*z* calc for $[C_{43}H_{55}ClN_2Pt + H]^+$: 831.3778. Found: 831.3796. Anal. Calc for $C_{43}H_{55}ClN_2Pt\cdot0.25$toluene: C, 62.98; H, 6.73; N, 3.28. Found: C, 62.68; H, 6.93; N, 3.37.

5. 287 mg yellow powder was obtained (yield: 61%). ^{1}H NMR ($CDCl_3$, 400 MHz): 9.16 − 9.19 (m, 1H), 8.24 (m, 1H), 8.16 (d, *J* = 7.6 Hz, 2H), 8.02 − 8.07 (m, 2H), 7.95 (d, *J* = 8.0 Hz, 1H), 7.83 − 7.87 (m, 1H), 7.49 − 7.66 (m, 5H), 7.34 − 7.44 (m, 5H), 7.26 − 7.31 (m, 2H), 1.94 − 2.10 (m, 4H), 0.54 − 0.97 (m, 30H). ESI-HRMS: *m*/*z* calc. for $[C_{51}H_{54}ClN_3Pt+H]^+$: 940.3733; Found, 940.3729. Anal. Calc. for $C_{51}H_{54}ClN_3Pt$: C, 65.20; H, 5.79; N, 4.47; Found: C, 64.94; H, 6.08; N, 4.44.

6. 287 mg of red powder was obtained (yield: 61%). ^{1}H NMR ($CDCl_3$, 400 MHz): 9.19−9.22 (m, 1H), 8.02−8.06 (m, 2H), 7.89−7.91 (d, *J* = 8.0 Hz, 1H), 7.77−7.82 (td, *J* = 8.0, 2.0 Hz, 1H), 7.68−7.71 (m, 1H), 7.62−7.66 (m, 1H), 7.48−7.52 (t, *J* = 8.4 Hz, 2H), 7.19−7.26 (m, 5H), 6.96−7.10 (m, 8H), 1.78−1.93 (m, 4H), 0.49−1.02 (m, 30H). ESI-HRMS: *m*/*z* calc for $[C_{51}H_{56}ClN_3Pt + H]^+$: 942.3889. Found: 942.3878. Anal. Calc for $C_{51}H_{56}ClN_3Pt$: C, 65.06; H, 5.99; N, 4.46. Found: C, 64.71; H, 6.25; N, 4.43.

Crystallographic Analysis. Single crystals of complex **1** were obtained by slow diffusion of hexane into the dilute dichloromethane solution of **1**. Single crystal X-ray diffraction data of **1** were collected on a Bruker Apex Duo diffractometer with an Apex 2 CCD area detector at *T* = 100 K. Mo radiation was used. All structures were processed with an Apex 2 v2010.9-1 software package (SAINT v. 7.68A, XSHELL v. 6.3.1).[21] A direct method was used to solve the structure after multiscan absorption corrections. Details of data collection and refinement are given in Table 1.

Photophysical Measurements. The solvents used for photophysical experiments were spectroscopic grade and were purchased from VWR International and used as is without further purification. An Agilent 8453 spectrophotometer was used to record the UV−vis absorption spectra in different solvents. A SPEX fluorolog-3 fluorometer/phosphorometer was used to measure the steady-state emission spectra in different solvents. The emission quantum yields were determined by the relative actinometry method[22] in degassed solutions, in which a degassed aqueous solution of $[Ru(bpy)_3]Cl_2$ ($\Phi_{em} = 0.042$, $\lambda_{ex} = 436$ nm)[23] was used as the reference for complexes **1**−**6**, and a degassed 1 N sulfuric acid solution of quinine bisulfate ($\Phi_{em} = 0.546$, $\lambda_{ex} = 347.5$ nm)[24] was used as the reference for ligands **1-L**−**6-L**.

The nanosecond transient difference absorption (TA) spectra and decays were measured in degassed solutions on an Edinburgh LP920 laser flash photolysis spectrometer. The third harmonic output (355 nm) of a Nd:YAG laser (Quantel Brilliant, pulse width: 4.1 ns, repetition rate was set at 1 Hz) was used as the excitation source. Each sample was purged with argon for 30 min prior to measurement. The triplet excited-state absorption coefficient (ε_T) at the TA band maximum was determined by the singlet depletion method.[25] After obtaining the ε_T value, the Φ_T could be determined by the relative actinometry using SiNc in benzene as the reference ($\varepsilon_{590} = 70000$ M^{-1} cm^{-1}, $\Phi_T = 0.20$).[26]

Nonlinear Transmission Experiment. The reverse saturable absorption of complexes **1**−**6** was characterized by a nonlinear transmission experiment at 532 nm using a Quantel Brilliant laser as the light source. The pulse width of the laser was 4.1 ns, and the repetition rate was set at 10 Hz. The complexes were dissolved in CH_2Cl_2. The concentration of the sample solutions was adjusted to obtain a linear transmission of 90% at 532 nm in a 2-mm-thick cuvette. The experimental setup and details are similar to those reported previously.[8b] A 40-cm plano-convex lens was used to focus the beam to the center of the 2-mm-thick sample cuvette. The radius of the beam waist at the focal point was approximately 96 μm.

Computational Details. The ground-state properties of complexes **1**−**6** were studied using density functional theory (DFT), while the excited states were simulated using linear response time-dependent DFT (TDDFT). All calculations—the geometry optimization, the ground-state and excited-state electronic structures, and optical spectra—were performed using the Gaussian 09 quantum chemistry software package.[27] All procedures were done utilizing the long-rang corrected functional CAM-B3LYP.[28] The LANL08 basis set[29] was used for the heavier Pt atom, while the remaining atoms were modeled with the 6-31G* basis set. The chosen method represents one of the currently most accurate DFT functionals and basis sets that have already shown good agreement with experimental data for different organometallic complexes.[30] All calculations have been performed in solvent using the conductor polarized continuum model (CPCM),[31] as implemented in Gaussian 09. Dichloromethane (CH_2Cl_2, $\varepsilon_r = 9.08$) was chosen as the solvent for consistency with the experimental studies. Implementation of solvent also helps to avoid any unnatural charge transfer states within the energy gap of these complexes.[32]

The excited-state energies and oscillator strengths have been studied using the linear response TDDFT formalism,[33] in which the adiabatic approximation for the exchange-correlation kernel was used. These calculations were done using the same basis sets and functional as used in the ground-state DFT calculations. For absorption spectra, the 40 lowest singlet optical transitions were considered to reach the transition energies of ~5 eV (250 nm). Each spectral line obtained from the TDDFT calculation was broadened by a Gaussian function with the line width of 0.1 eV to match the experimentally observed homogeneous broadening. The phosphorescence energies were calculated by first optimizing the lowest triplet state geometry followed by the vertical triplet excitations calculated via TDDFT.

In order to analyze the nature of the singlet and triplet excited states, natural transition orbital (NTO) analysis was performed based on the calculated transition densities.[34] This method offers the most compact representation of the transition density between the ground and excited states in terms of an expansion into single-particle transitions (hole and electron for each given excited state). Here we refer to the unoccupied NTO as the "electron" transition orbital and the occupied NTO as the "hole" transition orbital. NTOs shown in this paper were produced with the isovalue of 0.02 and visualized with the GaussView 5.1 graphical software.[35]

■ RESULTS AND DISCUSSION

Crystal Structure of 1. Single crystals of complex **1** were obtained by slow diffusion of hexane into the dichloromethane solution of **1**. The crystal structure and packing pattern are illustrated in Figure 1, and selected bond lengths, bond angles, and torsion angles are compiled in Table 2. As shown in Figure 1, two diastereomers (Figure 1a: *R* configuration at C25, 52%; Figure 1b: *S* configuration at C25, 48%) were observed in the crystal, which could arise from the racemic starting material 2-ethylhexyl bromide. In contrast, only the *S* configuration of C33 was observed. Nevertheless, the configuration of C25 or C33 plays a negligible role on the photophysics and nonlinear absorption of the Pt(II) complexes and thus is not the focus of this study. As a result, we only pick the diastereomer with *R* configuration at C25 (Figure 1a) for structural and packing discussion. The packing pattern is illustrated by two single cells viewed along the *b* axis in Figure 1c. Regardless of the two alkyl chains at the 9-position of the fluorene motif, the complex basically has a planar structure, in which bipyridine, Pt−Cl, fluorene, and nitro sit roughly in the same plane. The geometry

Table 2. Selected Bond Lengths, Bond Angles, and Torsion Angles of Complex 1

atom 1	atom 2	atom 3	atom 4	bond length/Å or bond angle/deg
Pt	Cl			2.296(1)
Pt	N1			1.944(3)
Pt	N2			2.101(3)
Pt	C23			1.986(3)
N1	C10			1.364(4)
N1	C6			1.349(4)
N2	C5			1.359(5)
N2	C1			1.342(4)
C5	C6			1.484(5)
C10	C11			1.467(5)
Cl	Pt	N1		178.49(9)
Cl	Pt	N2		98.42(8)
Cl	Pt	C23		98.97(11)
N1	Pt	N2		80.14(11)
N1	Pt	C23		82.48(13)
N2	Pt	C23		162.56(13)
Pt	N1	C10		117.8(2)
Pt	N1	C6		118.7(2)
C10	N1	C6		123.5(3)
Pt	N2	C5		112.2(2)
Pt	N2	C1		128.3(2)
C5	N2	C1		119.5(3)
Pt	C23	C11		112.3(3)
Pt	C23	C22		129.5(3)
C23	C11	C10		115.0(3)
Cl	Pt	N1	C10	−164(3)
N2	Pt	N1	C10	179.1(3)
C23	Pt	N1	C10	0.5(2)
N1	C6	C5	N2	0.6(4)
C23	C11	C10	N1	−0.6(4)

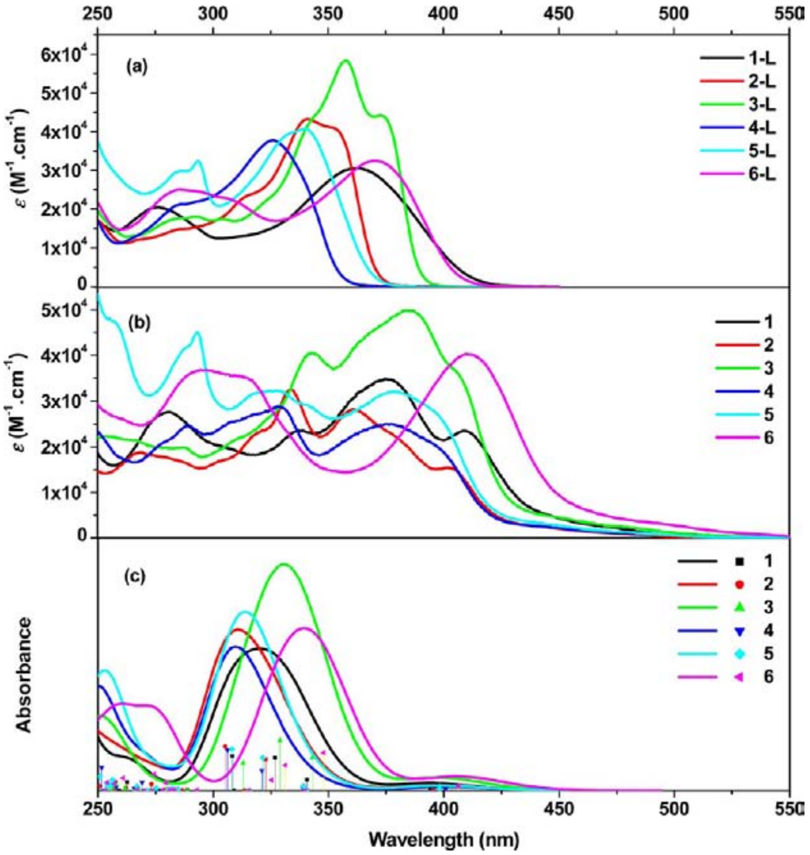

Figure 2. (a) UV−vis absorption spectra of ligands **1-L**−**6-L** measured in CH_2Cl_2. (b) UV−vis absorption spectra of complexes **1**−**6** measured in CH_2Cl_2. (c) Calculated absorption spectra for complexes **1**−**6**; vertical lines resemble excited states and the corresponding oscillator strength.

optimization of the molecule performed by DFT calculations also results in the planar configurations (Supporting Information Table S1).

The bond lengths of Pt−N1 (1.944(3) Å), Pt−N2 (2.101(3) Å), and Pt−C23 (1.986(3) Å) resemble our previously published data for a similar core structure in ref 11, with the corresponding values for complex **1** in ref 11 being 1.980(7) Å, 2.112(8) Å, and 1.997(8) Å, respectively.[11] The shorter bond length of Pt−N1 in this work is probably due to the weaker trans effect of chloride ligand compared to 4-tolylacetylide coligand in ref 11. The bond angles around the platinum center, Cl−Pt−C23 (98.97(11)), Cl−Pt−N2 (98.42(8)), N1−Pt−C23 (82.48(13)), and N1−Pt−N2 (80.14(11)), reveal deviation of the structure from an ideal square planar configuration around the metal center. The torsion angle between the fluorene and bipyridine components is approximately 0.6 deg (revealed by the torsion angle of C23−C11−C10−N1), while the NO_2 plane deviates from the fluorene plane by an angle of 6.5 deg (see the torsion angle of O1−N3−C17−C18).

Four molecules of **1** form a single centrosymmetric cell in the crystal matrix. In every single cell, two molecules adopt a head-to-tail packing with their π-conjugated planes opposite to each other; while the other two are in the perpendicular direction of the two packing molecules. The average distance between the two packing π-conjugated planes, defined by the distance of the two planes averaging the 26 atoms within the ring system of each molecule, is 3.306 Å, indicating the presence of $\pi-\pi$ interactions between the two molecules in the crystal matrix. The nearest Pt···Pt separation is 4.902 Å, which is longer than the Pt···Pt association range of 3.09−3.71 Å.[36] Therefore, no intermolecular Pt···Pt interactions are present even if in the crystal form.

Electronic Absorption. The electronic absorption spectra of ligands **1L**−**6L** and complexes **1**−**6** at different concentrations are recorded in dichloromethane solutions. The absorptions of these compounds obey Beer's Law in the concentration range of 1×10^{-6} to 1×10^{-4} mol/L, indicating the absence of ground-state aggregation in the concentration range studied in dichloromethane. As shown in Figure 2a, **1L**−**6L** display intense absorption bands from 300 to 400 nm, which predominantly arise from the $^1\pi,\pi^*$ transitions. However, contribution from intraligand charge transfer cannot be completely ruled out. The predominant $^1\pi,\pi^*$ character of these absorption bands is supported by the minor solvatochromic effect in these ligands, as demonstrated in Supporting Information Figures S1−S6. Comparing to **4-L**, the major absorption bands of all other ligands are red-shifted, which is likely the sign of electron delocalization induced by the substituent. A stronger electron-withdrawing substituent (NO_2 in **1-L**) and stronger electron-donating substituent (NPh_2 in **6-L**) cause the largest red-shift of the absorption band. Extended π-conjugation from the BTZ substituent in **3-L** also induces a significant red-shift and enhanced extinction coefficient.

For complexes **1**−**6**, the UV−vis absorption spectra consist of intense absorption bands below 420 nm and a broad tail above 420 nm (see spectra in Figure 2b). The intense absorption bands below 420 nm in complexes **1**−**3** (which contain electron-withdrawing substituents at the 7-position of fluorene) exhibit more featured spectra with a few well-distinct

Table 3. Experimental and Calculated Electronic Absorption Parameters for Complexes **1**–**6** and Experimental Absorption Data for Ligands **1-L**–**6-L** in CH_2Cl_2

	λ_{abs}/nm (ε_{max}/$M^{-1}\cdot cm^{-1}$)[a]	$^{Theor}\lambda_{abs}$/nm (S_n; f_{osc})[b]
1	409 (23430), 375 (34850), 339 (23530)	394 (S_1; 0.0563), 341 (S_2; 0.0094), 340 (S_3; 0.228), 327 (S_4; 0.679), 308 (S_6; 0.710)
2	402 (15400), 361 (28200), 334 (32530)	395 (S_1; 0.0416), 340 (S_2; 0.0091), 339 (S_3; 0.103), 323 (S_4; 0.649), 305 (S_7; 0.914)
3	404 (37320), 385 (49820), 343 (40510)	398 (S_1; 0.096), 343 (S_2, 0.692), 341 (S_3; 0.009), 329 (S_4; 1.047), 313 (S_6; 0.572)
4	376 (24930), 329 (28780)	400 (S_1; 0.0280), 340 (S_2; 0.0096), 339 (S_3; 0.0575), 321 (S_4; 0.420), 306 (S_6; 0.8470)
5	379 (31980), 328 (32330)	398 (S_1; 0.0382), 340 (S_2; 0.0097), 339 (S_3; 0.0966), 321 (S_4; 0.682), 308 (S_6; 0.863)
6	411 (40130), 310 (35550)	406 (S_1; 0.104), 348 (S_2; 0.782), 340 (S_3; 0.0103), 331 (S_4; 0.525)
1-L	362 (30540), 276 (20490)	
2-L	341 (43250)	
3-L	373 (44200), 358 (58250)	
4-L	326 (37730)	
5-L	340 (40650)	
6-L	370 (32500), 285 (25000)	

[a] λ_{abs} is absorption wavelength, ε_{max} is molar extinction coefficient. [b] $^{Theor}\lambda_{abs}$ is calculated wavelength corresponding to the transition between the ground and excited states of interest (number of excited states is shown in parentheses); f_{osc} is the calculated oscillator strength for the corresponding excitations.

peaks than those in complexes **4**–**6**, whic contain an electron-donating substituent. Similar to the trend observed in their corresponding ligands, the UV–vis absorption spectra for complexes with stronger electron-withdrawing or -donating substituents (complexes **1** and **6**) and with a BTZ substituent (complex **3**) are red-shifted compared to the other three complexes. This trend is well reproduced by our TDDFT calculations illustrated in Figure 2c and listed in Table 3, although the energies of all complexes are blue-shifted with respect to experimental data due to a high portion of the Hartree–Fock exchange in the CAM-B3LYP functional. The natural transition orbitals (NTOs) listed in Table 4 clearly indicate that the transitions contributing to the absorption bands around 400–410 nm and 360–380 nm for **1**–**3** are featured by mixed ^{1}MLCT (dπ(Pt) → π*(bpy)), ^{1}LLCT (π(Cl) → π*(bpy)), $^1\pi,\pi^*$, and ^{1}ILCT (intraligand charge transfer) characters, while the band at ca. 340 nm primarily arises from the mixed $^1\pi,\pi^*$/^{1}ML′CT (dπ(Pt) → π*(fluorene)) transitions. In contrast, the major absorption bands for **4** and **5** (with weak or moderate electron-donating substituents at the 7-position of fluorene) originate from the ^{1}MLCT/$^1\pi,\pi^*$/^{1}ILCT transitions, while complex **6**, with a strong electron-donating substituent, is featured predominantly with $^1\pi,\pi^*$/^{1}MLCT transitions in its major absorption band at ca. 410 nm, with a minor contribution from ^{1}LLCT/^{1}ILCT in its high-energy shoulder around 380 nm (see NTOs in Table 4). Such a pronounced $^1\pi,\pi^*$ character of optical transitions at ~410 nm is a result of the NPh_2 substituent in complex **6** that strongly delocalizes both the hole and electron orbitals via spreading the charge density toward the NPh_2 group. Increase in π-conjugation provides the most pronounced red-shift in the main absorption band of **6**, compared to those in complexes **4** and **5**, in which the electron is primarily localized on the bpy component, while the hole is spread over the fluorene motif. Note that although, for all complexes except **6**, the substituents are not directly involved in the NTOs contributing to the lower-energy edge of the main absorption band (380–420 nm), they play an important role in overall delocalization of the charge density over fluorene. Thus, the large red-shift of complex **3** is also associated with the increase in π-conjugation due to the substituent, which tends to partially spread both the hole and electron charge density over fluorene toward the BTZ substituent. The same trend is also noticeable (but less pronounced) in complex **1** with the strong electron-withdrawing substituent pulling the charge density to the fluorene, which explains its red-shift with respect to complex **2**.

In addition to the major absorption bands, a well pronounced tail appears at the low-energy end of the major absorption bands and extends to 550 nm in the absorption spectra of complexes **1**–**6**, as seen in Figure 2b and c. These tails become more distinguishable from the major absorption bands in MTHF, toluene, and hexane (see Supporting Information Figures S7– S12). The calculated NTOs contributing to the lowest-energy, low-intensity transition (Table 5) reveal that this tail features ^{1}MLCT/$^1\pi,\pi^*$/^{1}ILCT characters for all complexes. However, in accordance with the trend observed from the major absorption bands, this tail bathochromically shifts to longer wavelengths in complexes **1**, **3**, and **6** compared to those in **2**, **4**, and **5**, with the most pronounced red-shift and the highest intensity in complex **6**, due to the strongest delocalization of NTOs over the fluorene promoted by the strongest electron-donating NPh_2 group (Table 5).

Photoluminescence. Photoluminescence of ligands **1-L**–**6-L** and Pt(II) complexes **1**–**6** was studied at room temperature in different solvents and at 77 K in a butyronitrile glassy matrix. The spectra are presented in Figures 3 and 4 and in Supporting Information Figures S13–S20. The emission parameters are summarized in Table 6 and in Supporting Information Tables S2 and S3. As shown in Figure 3a and in Tables 6 and S2, ligands **3-L**–**6-L** exhibit intense fluorescence in all solvents in the region of 350–550 nm with the emission quantum yield in the range of 0.50–0.91. The emissions of **1-L** and **2-L** at room temperature are much weaker in comparison to those of **3-L**–**6-L**. Ligand **1-L** exhibits dual emission in CH_2Cl_2 solution when excited at 325 nm, with a slightly structured $^1\pi,\pi^*$ fluorescence at ca. 414 nm and a structureless ^{1}ILCT fluorescence at ca. 480 nm. When excited at 400 nm, only the ^{1}ILCT fluorescence is observed. The charge transfer nature of the 480 nm band is supported by the positive solvatochromic effect of this emission band and by the fact that this emission band is only observed in polar solvents such as CH_2Cl_2 and CH_3CN (Figure 4a). For **2-L**, only the $^1\pi,\pi^*$ fluorescence was observed in all of the solvents when excited below 330 nm. However, ^{1}ILCT was detected in CH_3CN solution when excited at 374 nm. The absence of charge transfer emission in solvents other than CH_3CN implies a weaker admixture of the ^{1}ILCT character in the lowest singlet excited state in **2-L** compared to **1-L**. This is reasonable because of the weaker electron-withdrawing ability of the formyl substituent with respect to the nitro substituent. In contrast, **3-L** only displays $^1\pi,\pi^*$ fluorescence with clear vibronic structure independent of the solvent polarity and the excitation wavelength. This feature can be attributed to the

Table 4. Natural Transition Orbitals (NTOs)[a] Representing Transitions That Correspond to the Main Absorption Bands for Complexes 1−6

	Excited state and properties	Hole	Electron		Excited state and properties	Hole	Electron
1	$\mathbf{S_3}$ $f_{\text{osc}} = 0.2279$ 340 nm	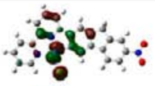	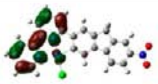				
	$\mathbf{S_4}$ $f_{\text{osc}} = 0.6786$ 327 nm	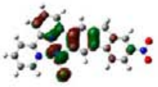	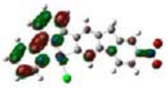	**4**	$\mathbf{S_4}$ $f_{\text{osc}} = 0.4201$ 321 nm	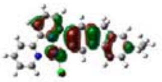	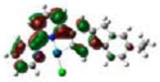
	$\mathbf{S_6}$ $f_{\text{osc}} = 0.7102$ 308 nm	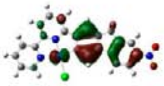			$\mathbf{S_6}$ $f_{\text{osc}} = 0.8470$ 306 nm	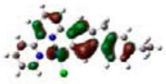	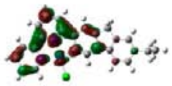
2	$\mathbf{S_3}$ $f_{\text{osc}} = 0.1034$ 339 nm	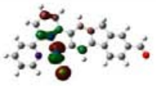	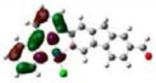				
	$\mathbf{S_4}$ $f_{\text{osc}} = 0.6492$ 323 nm	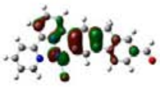	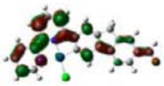	**5**	$\mathbf{S_4}$ $f_{\text{osc}} = 0.6820$ 321 nm		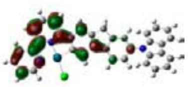
	$\mathbf{S_7}$ $f_{\text{osc}} = 0.9140$ 305 nm	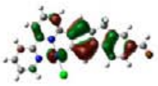	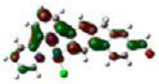		$\mathbf{S_6}$ $f_{\text{osc}} = 0.8630$ 308 nm		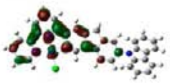
3	$\mathbf{S_2}$ $f_{\text{osc}} = 0.6915$ 343 nm	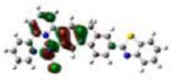	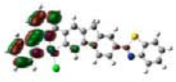	**6**	$\mathbf{S_2}$ $f_{\text{osc}} = 0.7823$ 348 nm		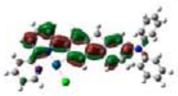
	$\mathbf{S_4}$ $f_{\text{osc}} = 1.0472$ 329 nm	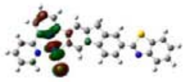	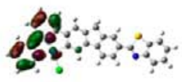		$\mathbf{S_4}$ $f_{\text{osc}} = 0.5252$ 331 nm	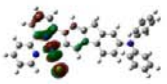	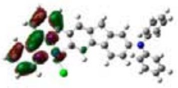
	$\mathbf{S_6}$ $f_{\text{osc}} = 0.5719$ 313 nm		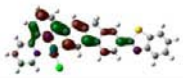				

[a] Note that excited-state NTOs differ from the ground-state MOs, and rather can be considered as the linear combination of the ground-state MOs that contribute to a given excited state.

Table 5. Natural Transition Orbitals Contributing to the Lowest-Energy Absorption "Tail" for Complexes 1−6

	Excited state number and properties	Hole	Electron
1	$\mathbf{S_1}$ $f_{\text{osc}} = 0.0563$ 394 nm	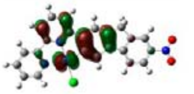	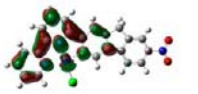
2	$\mathbf{S_1}$ $f_{\text{osc}} = 0.0416$ 395 nm		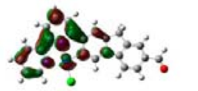
3	$\mathbf{S_1}$ $f_{\text{osc}} = 0.096$ 398 nm	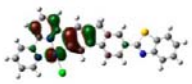	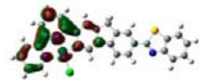
4	$\mathbf{S_1}$ $f_{\text{osc}} = 0.0280$ 400 nm	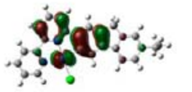	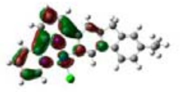
5	$\mathbf{S_1}$ $f_{\text{osc}} = 0.0382$ 398 nm		
6	$\mathbf{S_1}$ $f_{\text{osc}} = 0.1044$ 406 nm		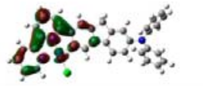

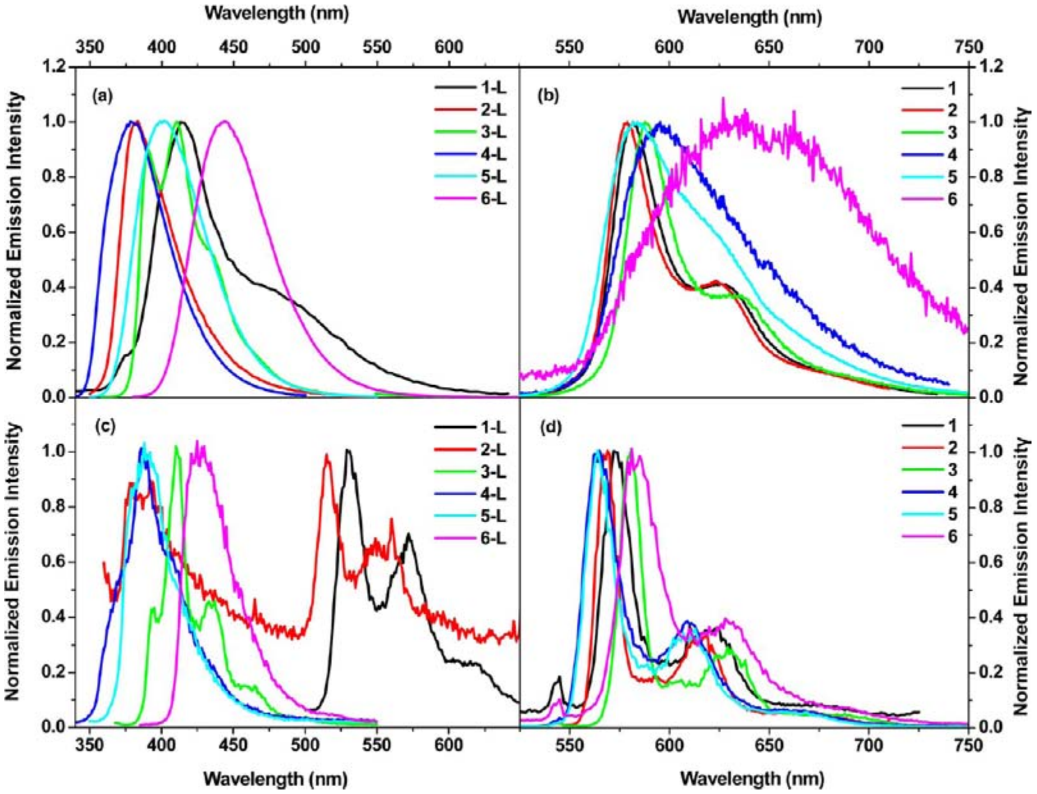

Figure 3. (a) Normalized emission spectra of ligands **1-L**−**6-L** (λ_{ex} was 325 nm for **1-L**, 320 nm for **2-L**, 348 nm for **3-L**, 326 nm for **4-L**, 340 nm for **5-L**, and 370 nm for **6-L**) in CH_2Cl_2 at the concentration of 1×10^{-5} mol/L for **2-L**−**6-L** and 5×10^{-4} mol/L for **1-L**. (b) Normalized emission spectra of complexes **1**−**6** (λ_{ex} was 372 nm for **1**, 360 nm for **2**, 383 nm for **3**, 375 nm for **4**, 380 nm for **5**, and 410 nm for **6**) in CH_2Cl_2 at the concentration of 1×10^{-5} mol/L. (c) Normalized emission spectra of **1-L**−**6-L** at 77 K in a glassy BuCN matrix (λ_{ex} was 405 nm for **1-L**, 350 nm for **2-L**, 358 nm for **3-L**, 326 nm for **4-L**, 340 nm for **5-L**, and 375 nm for **6-L**). (d) Normalized emission spectra of complexes **1**−**6** at 77 K in a glassy BuCN matrix at the concentration of 1×10^{-5} mol/L (λ_{ex} was 372 nm for **1**, 360 nm for **2**, 383 nm for **3**, 375 nm for **4**, 380 nm for **5**, and 410 nm for **6**).

extended π-conjugation induced by the BTZ substituent and the weaker electron-withdrawing ability of the BTZ substituent.

The emission characteristics of **4-L**−**6-L** (all with electron-donating substituents) at room temperature are quite similar. As exemplified in Figure 4b for **6-L**, the fluorescence spectrum becomes significantly red-shifted and featureless going from nonpolar solvents (hexane and toluene) to polar solvents (THF, CH_2Cl_2, CH_3CN), indicating a transition from $^1\pi,\pi^*$ fluorescence in nonpolar solvents to ^{1}ILCT fluorescence in polar solvents. The positive solvatochromic effect is more pronounced in **6-L** than in **5-L** and **4-L**, and the ^{1}ILCT emission energy apparently decreases from **4-L** to **5-L** to **6-L**. This trend is consistent with the strength of the electron-donating ability of the substituent in these compounds. With the increased electron-donating ability (i.e., NPh_2 > CBZ > *n*-Bu), the degree of intraligand (intramolecular) charge transfer is enhanced, which consequently induces the red-shift of the charge transfer emission.

The emission of **1-L**−**6-L** at 77 K in a butyronitrile glassy matrix was investigated in order to understand the phosphorescence from these compounds. As illustrated in Figure 3c, structured phosphorescence between 500 and 700 nm was observed only in **1-L** and **2-L**. The emission detected below 500 nm for **2-L**−**6-L** is low-temperature fluorescence, which becomes narrower, structured, and slightly blue-shifted due to the rigidochromic effect.[37]

Complexes **1**, **2**, and **3** exhibit well-structured emission at room temperature (Figure 3b) with the band maximum at 582, 579, and 588 nm, respectively, which show somewhat negative solvatochromic effect (as shown in Figure 4c for **2** and Figures S17 and S18 for **1** and **3**, respectively, in the Supporting Information). The vibronic progressions are 1208, 1220, and 1234 cm^{-1} for **1**, **2**, and **3**, respectively, and the emission lifetimes of **1**−**3** are in the range of 5.3−6.1 μs. These features suggest that the emissions of complexes **1**, **2**, and **3** emanate predominantly from the ligand-localized $^3\pi,\pi^*$ state. This assignment is confirmed by the calculated NTOs contributing to the lowest-energy triplet transition, as shown in Table 7. However, the calculated NTOs suggest that the emission of **1** and **2** has some contributions from the ^{3}MLCT states. In contrast, the emission spectra of **4**, **5**, and **6** are broad and less structured (or structureless for **6**) in CH_2Cl_2 solution at room temperature (as shown in Figure 3b), with apparently shorter lifetimes (i.e., 1.33 μs for **4** and 2.10 μs for **5**; and the lifetime for **6** was unable to be measured due to very weak signal) and lower quantum yields (see Table 6). The emission of **4** and **5** shows a negative solvatochromic effect in different solvents, as shown in Figure 4d for **5** and in Supporting Information Figure S19 for **4**. The emission of complex **6** was substantially quenched in polar solvents such as CH_2Cl_2 and CH_3CN. Taking all these facts into account, we conclude that the emission of **4**, **5**, and **6** has significant contribution from a triplet charge transfer state. Our TDDFT calculations confirm that the triplet transitions of complexes **4** and **5** admix ^{3}MLCT/$^3\pi,\pi^*$ characters, while the triplet transition of **6** primarily has ^{3}ILCT character, which is quite distinct from the

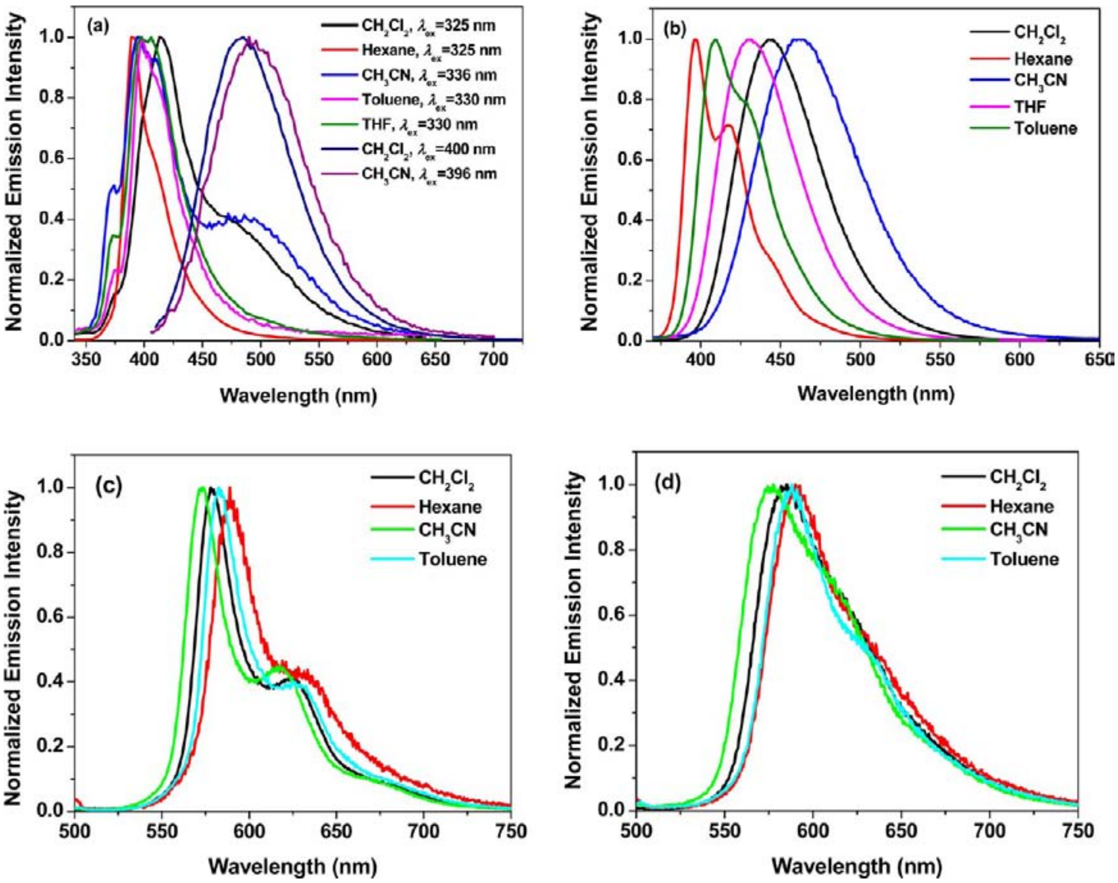

Figure 4. Normalized emission spectra of (a) **1-L**, (b) **6-L**, (c) **2**, and (d) **5** in different solvents. λ_{ex} = 360 nm for **6-L**, and λ_{ex} = 436 nm for **2** and **5**.

$^3\pi,\pi^*$ dominated character of the triplet transitions in complexes **1**−**3**, as illustrated in Table 7.

The emission of **1**−**6** at room temperature is concentration-dependent. As exemplified in Figure 5 for complex **1**, the emission intensity increases in the concentration range of 1×10^{-6} to 2×10^{-5} mol/L but decreases when the concentration is higher than 2×10^{-5} mol/L. Meanwhile, the emission lifetime keeps decreasing with increased concentration. Both facts suggest the occurrence of self-quenching in these complexes. The self-quenching rate constants deduced for **1**−**6** are provided in Table 6, which are on the order of 10^9 L·mol^{-1}·s^{-1} and are in line with those reported in the literature for other Pt(II) terdentate or diimine complexes.[8b,c,38] On the other hand, in view of the strong absorption at the respective excitation wavelength of each complex, the reduced emission intensity at high concentrations should also have contribution from a primary inner-filter effect.

The emission of **1**−**6** at 77 K was investigated in a butyronitrile glassy matrix, and the results are provided in Figure 3d and in Table 6. The emission spectra at 77 K for all complexes are blue-shifted, are more structured, and become narrower with respect to their corresponding emission spectra at room temperature, reflecting the rigidochromic effect.[37] The thermally induced Stokes shifts are 270 cm^{-1} for **1**, 304 cm^{-1} for **2**, 205 cm^{-1} for **3**, 892 cm^{-1} for **4**, 607 cm^{-1} for **5**, and 1479 cm^{-1} for **6**. The much smaller thermally induced Stokes shifts for **1**−**3** are consistent with the $^3\pi,\pi^*$ dominated nature of the emission, and the large Stokes shift for **6** is in accordance with the charge transfer character in the emitting triplet excited state. The moderate Stokes shifts in **4** and **5** also reflect the mixed ^{3}MLCT/$^3\pi,\pi^*$ characters in their emitting states.

Transient Absorption. The nanosecond transient absorption (TA) measurements were conducted for ligands **1-L**−**6-L** and complexes **1**−**6**. The following information can be obtained through the TA experiments: (1) the spectral feature of the triplet excited-state absorption; (2) the spectral region where the excited state absorbs more strongly than the ground state (can be identified from the positive absorption band(s) of the TA spectrum); (3) the excited-state lifetime (can be deduced from the decay of the TA); and (4) the triplet excited-state quantum yield (can be determined by the relative actinometry).

The nanosecond TA spectra of ligands **1-L**−**6-L** at zero delay after excitation are illustrated in Figure 6a. All compounds exhibit moderate to strong transient absorption in the visible to the NIR spectral region. Two trends emerge by examining the shape of the TA spectra of these compounds. First, the TA band maxima of the compounds with electron-withdrawing substituents (**1-L**−**3-L**) are obviously red-shifted compared to those of **4-L**−**6-L**, which contain electron-donating substituents. Second, the TA spectra of **1-L**, **5-L**, and **6-L** consist of two major absorption bands with a relatively narrower band between 400 and 500 nm, and a broader band above 500 nm (see Figures S21, S25, and S26 of the Supporting Information). Considering these different features, we tentatively attribute the observed TA to the $^3\pi,\pi^*$ states for these compounds. However, for **1-L**, **5-L**, and **6-L**, ^{3}ILCT could also contribute significantly to the observed TA in view of the facile intraligand

Table 6. Emission and Excited-State Absorption Parameters for Complexes 1–6 and Ligands 1-L–6-L

	λ_{em}/nm (τ_0/μs; k_{sq}/L·mol^{-1}·s^{-1}); Φ_{em} ^{a}	λ_{em}/nm (τ_{em}/μs)^b	$\lambda_{T_1-T_n}$/nm (τ_T/μs; $\varepsilon_{T_1-T_n}$/M^{-1} cm^{-1}; Φ_T)^c	$^{theor}\lambda_{phos}$/nm
	RT	77 K		
1	582 (6.0; 2.04 × 10^9), 626 (6.2; 1.83 × 10^9); 0.077	573 (15.7), 621 (16.0)	655 (6.1; 18530; 0.56)	621
2	579 (5.3; 1.46 × 10^9), 623 (5.5; 1.62 × 10^9); 0.11	569 (19.3), 617 (19.3)	580 (5.5; 27910; 0.40)	621
3	588 (6.1; 1.44 × 10^9), 634 (6.1; 9.33 × 10^8); 0.092	581 (24.0), 630 (28.0)	625 (8.2; 56980; 0.33)	634
4	595 (1.3; 3.49 × 10^9); 0.031	565 (22.1), 610 (20.0)	555 (2.1; 14870; 0.50)	600
5	584 (2.1; 2.00 × 10^9); 0.06	564 (21.5), 609 (21.2)	560 (3.8; 13170; 0.32)	601
6	638 (−); 0.003	583 (24.9), 629 (20.9)	530 (1.4; 35680; 0.38), 755 (1.1; 20990; 0.38)	618
1-L	414 (−), 483 (−); −	530, 572	655 (18.6; −; −)	
2-L	383 (−); 0.066	378, 515, 549	535 (4.9; −; −)	
3-L	410 (−); 0.80	410	580 (5.4; −; −)	
4-L	378 (−); 0.69	385	520 (10.1; −; −)	
5-L	401 (−); 0.91	388	445 (10.0; −; −)	
6-L	444 (−); 0.84	425	460 (−; −; −)	

[a] Emission wavelength (λ_{em}), intrinsic lifetime (τ_0), self-quenching rate constant (k_{sq}), and emission quantum yield measured in CH_2Cl_2. [b] In BuCN glassy matrix. [c] Triplet excited-state absorption band maximum ($\lambda_{T_1-T_n}$), molar extinction coefficient ($\varepsilon_{T_1-T_n}$), quantum yield (Φ_T), and lifetime (τ_T) measured in CH_3CN for **1**–**5**; **6** was measured in toluene.

charge transfer that could admix the ^{3}ILCT character into the $^3\pi,\pi^*$ states.

Figure 6b shows the TA spectra of complexes **1**–**6** at zero delay after excitation. The time-resolved TA spectrum of **1** is illustrated in Figure 6c, while the others are provided in Figures S27–S31 of the Supporting Information. The TA spectra for all complexes feature two major absorption bands, a narrower one between 400 and 500 nm and a broader one above 500 nm. The low-energy TA bands are stronger than the 400–500 nm absorption bands in **1**–**3**, but the relative intensity of these two bands is opposite in **4**–**6**. Compared to the TA spectra of their respective ligands, the low-energy absorption bands of the TA spectra for these complexes are red-shifted, indicating electron delocalization induced by the interaction of the Pt(II) center with the ligand. For all complexes, bleaching occurs at $\lambda < 430$ nm, which is consistent with the position of the major absorption band in their respective UV–vis absorption spectra. The triplet lifetimes deduced from the decay of the TA (Table 6) for these complexes are similar to those obtained from the decay of emission, implying that the excited state giving rise to the observed TA could be the same excited state that emits. On the basis of these features, we tentatively ascribe the TA of **1**–**5** as being predominantly from their $^3\pi,\pi^*$ states, with possible contributions from the ^{3}MLCT states for **1**, **2**, **4**, and **5**. For complex **6**, the TA in CH_3CN was too weak to be detected. However, a moderately strong TA spectrum was observed in toluene. The absence of TA in a polar solvent such as CH_3CN and the shorter lifetime (τ_T = 1.4 μs in toluene) suggest the charge transfer nature of the triplet excited state that gives rise to the observed TA. Considering the nature of the emitting state of **6** discussed earlier, we believe the TA of **6** predominantly arises from the ^{3}ILCT state.

Reverse Saturable Absorption. The TA spectra of **1**–**6** indicate that all complexes exhibit positive absorption at 532 nm, suggesting stronger excited-state absorption than that of the ground state. In addition, the triplet excited-state lifetimes for these complexes are much longer than the nanosecond laser pulse width (4.1 ns). These provide the necessary conditions for reverse saturable absorption (RSA, defined as a decreased transmission upon increase of incident energy) to occur for a nanosecond laser pulse at 532 nm. To demonstrate this, a nonlinear transmission experiment using complexes **1**–**6** at 532 nm for nanosecond laser pulses was carried out in CH_2Cl_2 solution at a linear transmittance of 90% in a 2-mm cuvette. For comparison purposes, the RSA of complex **1** in ref 11, which has a similar structure to that of complex **3** in this work but with a tolylacetylide coligand instead of a Cl coligand, was also measured under the same experimental conditions. The results are displayed in Figure 7. The transmission of the complexes drastically decreases with increased incident energy, a clear indication of strong RSA. The degree of RSA of these complexes increases in the order of **4** ≈ **5** < **1** ≈ **3** < **2** < **6**, and the RSA of **3** is slightly better than that of complex **1** in ref 11. It appears that the RSA is generally stronger in complexes with electron-withdrawing substituents (**1**–**3**) than in complexes with electron-donating substituents, except for **6**, which contains the strongest electron-donating substituent. The strongest RSA from **6** should be related to its stronger excited-state absorption at 532 nm, which is evident by its TA spectrum, in which one of the absorption bands occurs at ca. 530 nm.

To better rationalize the observed RSA trend of these complexes at 532 nm for nanosecond laser irradiation, the ratios of the excited-state absorption cross section (σ_{ex}) relative to the ground-state absorption cross section (σ_0) (which is a key parameter for RSA) at 532 nm for **1**–**6** have to be evaluated. The σ_{ex} values at 532 nm can be estimated from the ΔODs of the nanosecond TA at zero delay at 532 nm and at the TA band maximum ($\lambda_{T_1-T_n}$), from the ground-state absorbance (A) at 532 nm and at the TA band maximum of the same solution for the TA measurement, and from the molar extinction coefficient ($\varepsilon_{T_1-T_n}$) at the TA band maximum, as well as from the conversion equation $\sigma = 3.82 \times 10^{-21}\varepsilon$. The detailed procedure for the estimation of these values follows that described by our group previously.[8m] The σ_0 values at 532 nm can be deduced from the ground-state absorption molar extinction coefficients using $\sigma = 3.82 \times 10^{-21}\varepsilon$. The resultant σ_{ex} and σ_0 values as well as the ratios of σ_{ex}/σ_0 are compiled in Table 8. It is obvious that the σ_{ex}/σ_0 values follow the trend of **4** < **5** < **1** < **3** < **2** < **6**, which correlates very well with the trend of the RSA plots of these complexes. The correspondence between the σ_{ex}/σ_0 values and RSA performances indicates that the RSA mainly arises from the triplet excited states of the complexes. This notion is quite reasonable because the femtosecond TA study on complex **1** in ref 11 found that intersystem crossing from the singlet to triplet excited states occurs in ~88 ps ($\tau_{isc} = \tau_s/\Phi_T$); and during the nanosecond excitation, the triplet excited state is the dominant contributor based on the calculated fractional populations of the affected excited states.[11] Considering the similar core structure of

Table 7. Natural Transition Orbitals Representing the Lowest-Energy Triplet Transitions for Complexes 1–6

	Triplet Energy	Hole	Electron
1	2.00 eV (621 nm)		
2	2.00 eV (621 nm)	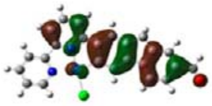	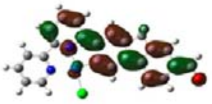
3	1.96 eV (634 nm)	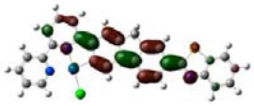	
4	2.07 eV (600 nm)		
5	2.06 eV (601 nm)		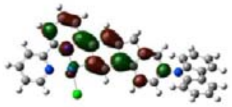
6	2.01 eV (618 nm)		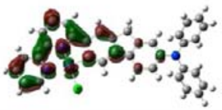

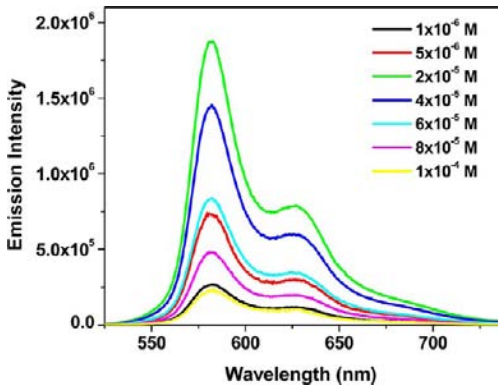

Figure 5. Concentration-dependent emission spectra of **1** in CH_2Cl_2. λ_{ex}= 372 nm.

complexes **1**–**6** to that of complex **1** in ref 11, it is reasonable to assume that the dominant contributing excited state to the RSA within the nanosecond pulse width should be the triplet excited states for **1**–**6** as well. Complex **6** possesses the strongest triplet excited-state absorption at 532 nm and thus the strongest RSA. The σ_{ex}/σ_0 value for complex **3** is also much larger than that for its counterpart with the tolylacetylide ligand (*i.e.* complex **1** in ref 11), which has σ_T/σ_0 = 69.6.[11] The much larger ratio for complex **3** should be mainly due to the significantly reduced ground-state absorption cross section of **3** at 532 nm ($\sigma_0 = 4.3 \times 10^{-19}$ cm^2) with respect to complex **1** in ref 11 ($\sigma_0 = 1.48 \times 10^{-18}$ cm^2). This confirms our initial design concept that replacing the tolylacetylide coligand with Cl coligand could reduce the ground-state absorption in the visible spectral region and thus increase the σ_{ex}/σ_0 ratio and enhance the RSA in the visible spectral region. It is also worth noting that the σ_{ex}/σ_0 ratios for **1**–**6** are much larger than those of most of the reverse saturable absorbers reported in the literature;[8b,c,h,i,f,11,38b,c,39] and the σ_{ex}/σ_0 value for **6** is among the largest values reported to date.

■ CONCLUSION

Six new Pt(II) complexes (**1**–**6**) containing 6-[9,9-di(2-ethylhexyl)-7-*R*-9*H*-fluoren-2-yl]-2,2′-bipyridine (R = NO_2, CHO, benzothiazol-2-yl, *n*-Bu, carbazol-9-yl, NPh_2) ligands were synthesized, and their photophysics were systematically investigated by spectroscopic techniques and TDDFT theoretical calculations. The absorption and emission characteristics of **1**–**6** can be substantially adjusted by the 7-substituent. It is found that electron-withdrawing substituents (NO_2, CHO, BTZ) and electron-donating substituents (*n*-Bu, CBZ, NPh_2) exert distinct effects on the photophysics of the complexes. The lowest-energy absorption bands of **1**–**6** all feature ^{1}MLCT/^{1}ILCT/$^1\pi,\pi^*$ characters, while the contributions of ^{1}MLCT, ^{1}LLCT, $^1\pi,\pi^*$, and ^{1}ILCT configurations to the major absorption band(s) vary depending on the nature of the substituent. The different substituents influence the nature of the lowest triplet excited states of **1**–**6** more distinctively, reflected by the fact that the emitting excited state of complexes **1**–**3** is dominated by the $^3\pi,\pi^*$ characters with a little contribution from ^{3}MLCT in **1** and **2**, while the emission of **4** and **5** admixes ^{3}MLCT/$^3\pi,\pi^*$ characters, and **6** primarily exhibits very weak ^{3}ILCT emission. It appears that the $^3\pi,\pi^*$ character diminishes while charge transfer character increases when the strength of the electron-donating substituent increases. All complexes exhibit broad and strong triplet excited-state absorption from the near-UV to the near-IR spectral region, which originates from the same triplet excited

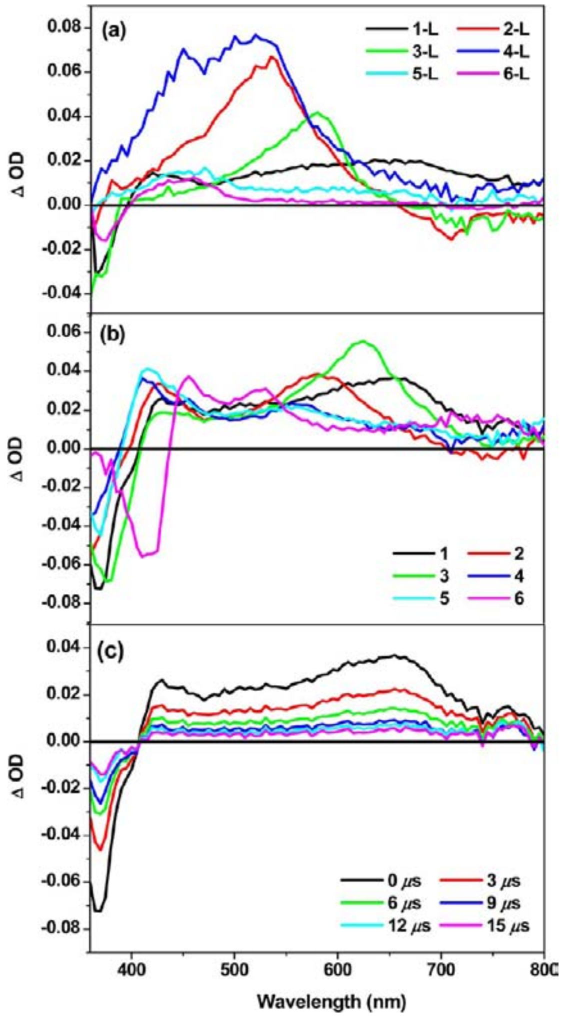

Figure 6. Nanosecond transient difference absorption spectra of (a) ligands **1-L** − **6-L** and (b) complexes **1** − **6** at zero delay after excitation; (c) time-resolved TA spectra of **1**. **1-L** − **5-L** and **1** − **5** were measured in CH_3CN, **6-L** and **6** were measured in toluene. λ_{ex} = 355 nm, A_{355} = 0.4 in a 1-cm cuvette.

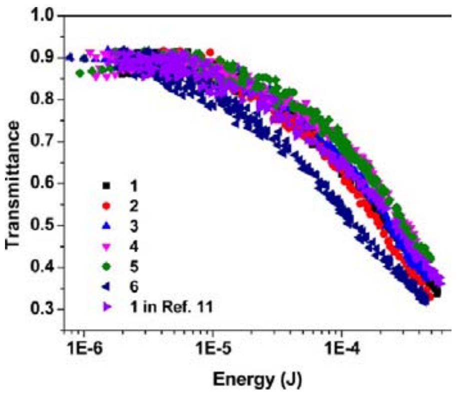

Figure 7. Nonlinear transmission curves for **1**−**6** and complex **1** in ref 11 in CH_2Cl_2 in a 2 mm cuvette for 4.1 ns laser pulses at 532 nm. The radius of the beam waist at the focal point was approximately 96 μm. The linear transmission for all samples was adjusted to 90% in a 2 mm cuvette.

state that emits. The TA band maxima are red-shifted for complexes **1**−**3** (which possess the electron-withdrawing substituents) compared to those of **4**−**6** (which contain electron-donating substituents). Due to the much stronger triplet excited-state absorption than the ground-state absorption of **1**−**6** in the visible spectral region, all complexes exhibit strong reverse saturable absorption for a nanosecond laser pulse at 532 nm, with complex **6** showing the strongest RSA due to its strongest excited-state absorption at 532 nm and thus the largest ratio of σ_{ex}/σ_0. The σ_{ex}/σ_0 ratios for the other five complexes are also much larger than most of the reverse saturable absorbers reported in the literature at 532 nm. This makes complexes **1**−**6**, especially **6**, very promising candidates for devices that require strong RSA.

Table 8. Ground-State (σ_0) and Excited-State (σ_{ex}) Absorption Cross Sections for Complexes 1−6 at 532 nm

	1	2	3	4	5	6
$\sigma_0/10^{-18}$ cm^{2a}	0.27	0.27	0.43	0.38	0.38	0.88
$\sigma_{ex}/10^{-18}$ cm^{2b}	46	67	80	44	46	230
σ_{ex}/σ_0	170	248	186	116	121	261

[a] In CH_2Cl_2. [b] **1**−**5** in CH_3CN and **6** in toluene.

■ ASSOCIATED CONTENT

Ⓢ Supporting Information

X-ray crystallographic data for complex **1** in CIF format, the synthetic procedures and ^1H NMR data of all the intermediates, the absorption spectra of **1-L**−**6-L** and **1**−**6** in different solvents, the emission spectra of **2-L**−**5-L** and **1**, **3**, **4**, and **6** in different solvents, the nanosecond time-resolved transient absorption spectra of **1-L**−**6-L** and **2**−**6**, the emission quantum yields of **1-L**−**6-L** and **1**−**6** in different solvents, and the optimized geometries of **1**−**6** via DFT calculations. This material is available free of charge via the Internet at http://pubs.acs.org.

■ AUTHOR INFORMATION

Corresponding Author

*E-mail: Wenfang.Sun@ndsu.edu. Phone: 701-231-6254. Fax: 701-231-8831.

Notes

The authors declare no competing financial interest.

■ ACKNOWLEDGMENTS

This work is partially supported by the National Science Foundation (CAREER CHE-0449598 and CHEM-0946990) and partially by the Army Research Laboratory (W911NF-06-2-0032 and W911NF-10-2-0055) to W. Sun. S. Kilina acknowledges the U.S. Department of Energy Early-Career Grant DE-SC008446 for financial support and North Dakota State University and the Center for Integrated Nanotechnology (CINT) at Los Alamos National Laboratory for computer access and administrative support.

■ REFERENCES

(1) Williams, J. A. G. *Top. Curr. Chem.* **2007**, *281*, 205.

(2) Dhar, S.; Lippard, S. J. In *Bioinorganic Medicinal Chemistry*; Enzo Alessio, Ed.; Wiley-VCH Verlag GmbH & Co. KGaA: Weinheim, Germany, 2010; Chapter 3, pp 79−95.

(3) (a) Chan, S. C.; Chan, M. C. W.; Wang, Y.; Che, C. M.; Cheung, K. K.; Zhu, N. *Chem.—Eur. J.* **2001**, *7*, 4180. (b) Lu, W.; Mi, B. X.; Chan, M. C. W.; Hui, Z.; Che, C. M.; Zhu, N.; Lee, S. T. *J. Am. Chem. Soc.* **2004**, *126*, 4958.

(4) Chakraborty, S.; Wadas, T. J.; Hester, H.; Flaschenreim, C.; Schmehl, R.; Eisenberg, R. *Inorg. Chem.* **2005**, *44*, 6865.

(5) Taranekar, P.; Qiao, Q.; Jiang, H.; Ghiviriga, I.; Schanze, K. S.; Reynolds, J. R. *J. Am. Chem. Soc.* **2007**, *129*, 8958.

(6) Kwok, E. C.-H.; Chan, M.-Y.; Wong, K. M.-C.; Lam, W. H.; Yam, V. W.-W. *Chem.—Eur. J.* **2010**, *16*, 12244.

(7) (a) Zhang, H.; Zhang, B.; Li, Y.; Sun, W. *Inorg. Chem.* **2009**, *48*, 3617. (b) Grove, L. J.; Rennekamp, J. M.; Jude, H.; Connick, W. B. *J. Am. Chem. Soc.* **2004**, *126*, 1594. (c) Mathew, I.; Sun, W. *Dalton Trans.* **2010**, *39*, 5885. (d) Ji, Z.; Li, Y.; Sun, W. *J. Organomet. Chem.* **2009**, *694*, 4140. (e) Lu, W.; Chan, M. C. W.; Zhu, N.; Che, C.-M.; He, Z.; Wong, K. Y. *Chem.—Eur. J.* **2003**, *9*, 6155. (f) Wong, K. M.; Tang, W.-S.; Lu, X.-X.; Zhu, N.; Yam, V. W.-W. *Inorg. Chem.* **2005**, *44*, 1492. (g) Yang, Q.-Z.; Wu, L.-Z.; Zhang, H.; Chen, B.; Wu, Z.-X.; Zhang, L.-P.; Tung, Z.-H. *Inorg. Chem.* **2004**, *43*, 5195.

(8) (a) Sun, W.; Zhang, B.; Li, Y.; Pritchett, T. M.; Li, Z.; Haley, J. E. *Chem. Mater.* **2010**, *122*, 6384. (b) Guo, F.; Sun, W.; Liu, Y.; Schanze, K. *Inorg. Chem.* **2005**, *44*, 4055. (c) Shao, P.; Li, Y.; Yi, J.; Pritchett, T. M.; Sun, W. *Inorg. Chem.* **2010**, *49*, 4507. (d) Ji, Z.; Li, Y.; Pritchett, T. M.; Makarov, N. S.; Haley, J. E.; Li, Z.; Drobizhev, M.; Rebane, A.; Sun, W. *Chem.—Eur. J.* **2011**, *17*, 2479. (e) Rogers, J. E.; Slagle, J. E.; Krein, D. M.; Burke, A. R.; Hall, B. C.; Fratini, A.; McLean, D. G.; Fleitz, P. A.; Cooper, T. M.; Drobizhev, M.; Makarov, N. S.; Rebane, A.; Kim, K.-Y.; Farley, R.; Schanze, K. S. *Inorg. Chem.* **2007**, *46*, 6483. (f) Pritchett, T. M.; Sun, W.; Guo, F.; Zhang, B.; Ferry, M. J.; Rogers-Haley, J. E.; Shensky, W., III; Mott, A. G. *Opt. Lett.* **2008**, *33*, 1053. (g) Shao, P.; Li, Y.; Sun, W. *J. Phys. Chem. A* **2008**, *112*, 1172. (h) Sun, W.; Zhu, H.; Barron, P. M. *Chem. Mater.* **2006**, *18*, 2602. (i) Liu, R.; Li, Y.; Li, Y.; Zhu, H.; Sun, W. *J. Phys. Chem. A* **2010**, *114*, 12639. (j) Liu, R.; Azenkeng, A.; Li, Y.; Sun, W. *Dalton Trans.* **2010**, *41*, 12353. (k) Liu, R.; Zhou, D.; Azenkeng, A.; Li, Z.; Li, Y.; Glusac, K. D.; Sun, W. *Chem.—Eur. J.* **2012**, *18*, 11440. (l) Zhang, B.; Li, Y.; Liu, R.; Pritchett, T. M.; Haley, J. E.; Sun, W. *ACS Appl. Mater. Interfaces* **2013**, *5*, 565. (m) Li, Y.; Liu, R.; Badaeva, E.; Kilina, S.; Sun, W. *J. Phys. Chem. C* **2013**, *117*, 5908. (n) Liu, R.; Dandu, N.; Li, Y.; Kilina, S.; Sun, W. *Dalton Trans.* **2013**, *42*, 4398. (o) Li, Z.; Badaeva, E.; Zhou, D.; Bjorgaard, J.; Glusac, K.; Killina, S.; Sun, W. *J. Phys. Chem. A* **2012**, *116*, 4878. (p) Liu, R.; Azenkeng, A.; Zhou, D.; Li, Y.; Glusac, K. D.; Sun, W. *J. Phys. Chem. A* **2013**, *117*, 1907. (q) Dubinina, G. G.; Price, R. S.; Abboud, K. A.; Wicks, G.; Wnuk, P.; Stepanenko, Y.; Drobizhev, M.; Rebane, A.; Schanze, K. S. *J. Am. Chem. Soc.* **2012**, *134*, 19346.

(9) Andrews, L. J. *J. Phys. Chem.* **1979**, *83*, 3203.

(10) McMillin, D. R.; Moore, J. J. *Coord. Chem. Rev.* **2002**, *229*, 113.

(11) Zhang, B.; Li, Y.; Liu, R.; Pritchett, T. M.; Azenkeng, A.; Ugrinov, A.; Haley, J. E.; Li, Z.; Hoffmann, M. R.; Sun, W. *Chem.—Eur. J.* **2012**, *18*, 4593.

(12) Maji, M. S.; Pfeifer, T.; Studer, A. *Chem.—Eur. J.* **2010**, *16*, 5872.

(13) Montes, V. A.; Perez-Bolivar, C.; Agarwal, N.; Shinar, J.; Anzenbacher, P., Jr. *J. Am. Chem. Soc.* **2006**, *128*, 12436.

(14) Van der Pol, C.; Bryce, M. R.; Wielopolski, M.; Atienza-Castellanos, C.; Guldi, D. M.; Filippone, S.; Martin, N. *J. Org. Chem.* **2007**, *72*, 6662.

(15) Peterson, J. J.; Werre, M.; Simon, Y. C.; Coughlin, E. B.; Carter, K. R. *Macromolecules* **2009**, *42*, 8594.

(16) Dudek, S. P.; Pouderoijen, M.; Abbel, R.; Schenning, A. P. H. J.; Meijer, E. W. *J. Am. Chem. Soc.* **2005**, *127*, 11763.

(17) Kannan, R.; He, G. S.; Yuan, L.; Xu, F.; Prasad, P. N.; Dombroskie, A. G.; Reinhardt, B. A.; Baur, J. W.; Vaia, R. A.; Tan, L.-S. *Chem. Mater.* **2001**, *13*, 1896.

(18) Fisher, A. L.; Linton, K. E.; Kamtekar, K. T.; Pearson, C.; Bryce, M. R.; Petty, M. C. *Chem. Mater.* **2011**, *23*, 1640.

(19) Sonntag, M.; Strohriegl, P. *Liq. Cryst.* **2007**, *34*, 49.

(20) Shin, D.; Switzer, C. *Chem. Commun.* **2007**, *42*, 4401.

(21) (a) Bruker Analytical X-ray Systems, Madison, WI, 2010. (b) Sheldrick, G. M. *Acta Crystallogr.* **2008**, *A64*, 112. (c) Blessing, R. H. *Acta Crystallogr.* **1995**, *A51*, 33.

(22) Demas, J. N.; Crosby, G. A. *J. Phys. Chem.* **1971**, *75*, 991.

(23) Van Houten, J.; Watts, R. *J. Am. Chem. Soc.* **1976**, *98*, 4853.

(24) Eaton, D. F. *Pure Appl. Chem.* **1988**, *60*, 1107.

(25) Carmichael, I.; Hug, G. L. *J. Phys. Chem. Ref. Data* **1986**, *15*, 1.

(26) Firey, P. A.; Ford, W. E.; Sounik, J. R.; Kenney, M. E.; Rodgers, M. A. J. *J. Am. Chem. Soc.* **1988**, *110*, 7626.

(27) Frisch, M. J.; Trucks, G. W.; Schlegel, H. B.; Scuseria, G. E.; Robb, M. A.; Cheeseman, J. R.; Scalmani, G.; Barone, V.; Mennucci, B.; Petersson, G. A.; Nakatsuji, H.; Caricato, M.; Li, X.; Hratchian, H. P.; Izmaylov, A. F.; Bloino, J.; Zheng, G.; Sonnenberg, J. L.; Hada, M.; Ehara, M.; Toyota, K.; Fukuda, R.; Hasegawa, J.; Ishida, M.; Nakajima, T.; Honda, Y.; Kitao, O.; Nakai, H.; Vreven, T.; Montgomery, J. A., Jr.; Peralta, J. E.; Ogliaro, F.; Bearpark, M.; Heyd, J. J.; Brothers, E.; Kudin, K. N.; Staroverov, V. N.; Kobayashi, R.; Normand, J.; Raghavachari, K.; Rendell, A.; Burant, J. C.; Iyengar, S. S.; Tomasi, J.; Cossi, M.; Rega, N.; Millam, N. J.; Klene, M.; Knox, J. E.; Cross, J. B.; Bakken, V.; Adamo, C.; Jaramillo, J.; Gomperts, R.; Stratmann, R. E.; Yazyev, O.; Austin, A. J.; Cammi, R.; Pomelli, C.; Ochterski, J. W.; Martin, R. L.; Morokuma, K.; Zakrzewski, V. G.; Voth, G. A.; Salvador, P.; Dannenberg, J. J.; Dapprich, S.; Daniels, A. D.; Farkas, Ö.; Foresman, J. B.; Ortiz, J. V.; Cioslowski, J.; Fox, D. J. *Gaussian 09*, Revision A.1; Gaussian, Inc.: Wallingford, CT, 2009.

(28) Yanai, T.; Tew, D.; Handy, N. *Chem. Phys. Lett.* **2004**, *393*, 51.

(29) Roy, L. E.; Hay, P. J.; Martin, R. L. *J. Comp. Theor. Chem.* **2008**, *4*, 1029.

(30) (a) Roy, L. E.; Scalmani, G.; Kobayashi, R.; Batista, E. R. *Dalton Trans.* **2009**, 6719. (b) Peach, M. J. G.; Benfield, P.; Helgaker, T.; Tozer, D. J. *J. Chem. Phys.* **2008**, *128*, 044118. (c) Vlček, A., Jr.; Záliš, S. *Coord. Chem. Rev.* **2007**, *251*, 258.

(31) (a) Barone, V.; Cossi, M.; Tomasi, J. *J. Comput. Chem.* **1998**, *19*, 404. (b) Cossi, M.; Rega, N.; Scalmani, G.; Barone, V. *J. Comput. Chem.* **2003**, *24*, 669.

(32) (a) Batista, E. R.; Martin, R. L. *J. Phys. Chem. A.* **2005**, *109*, 3128. (b) Fantacci, S.; De Angelis, F.; Selloni, A. *J. Am. Chem. Soc.* **2003**, *125*, 4381. (c) Filippo, D. A.; Simona, F.; Annabella, S. *Chem. Phys. Lett.* **2004**, *389*, 204.

(33) Furche, F.; Ahlrichs, R. *J. Chem. Phys.* **2002**, *117*, 7433.

(34) Martin, R. L. *J. Chem. Phys.* **2003**, *118*, 4775.

(35) Dennington, R., II; Keith, T.; Millam, J. *GaussView*, Version 4.1; Semichem Inc.: Shawnee Mission, KS, 2007.

(36) Stork, J. R.; Olmstead, M. M.; Balch, A. L. *Inorg. Chem.* **2004**, *43*, 7508.

(37) (a) Juris, A.; Balzani, V.; Barigelletti, F.; Campagna, S.; Belser, P.; Von Zelewsky, A. *Coord. Chem. Rev.* **1988**, *84*, 85. (b) Cummings, S. D.; Eisenberg, R. *J. Am. Chem. Soc.* **1996**, *118*, 1949. (c) Polo, A. S.; Itokazu, M. K.; Frin, K. M.; Patrocinio, A. O. de T.; Iha, N. Y. M. *Coord. Chem. Rev.* **2006**, *250*, 1669. (d) Lai, S.-W.; Chan, M. C. W.; Cheung, K.-K.; Che, C.-M. *Inorg. Chem.* **1999**, *38*, 4262.

(38) (a) Hissler, M.; Connick, W. B.; Geiger, D. K.; McGarrah, J. E.; Lipa, D.; Lachicotte, R. J.; Eisenberg, R. *Inorg. Chem.* **2000**, *39*, 447. (b) Shao, P.; Li, Y.; Sun, W. *Organometallics* **2008**, *27*, 2743. (c) Ji, Z.; Li, Y.; Sun, W. *Inorg. Chem.* **2008**, *47*, 7599. (d) Shao, P.; Li, Y.; Azenkeng, A.; Hoffmann, M.; Sun, W. *Inorg. Chem..* **2009**, *48*, 2407. (e) Lai, S.-W.; Chan, M. C.-W.; Cheung, T.-C.; Peng, S.-M.; Che, C.-M. *Inorg. Chem.* **1999**, *38*, 4046. (f) Yam, V. W.-W.; Tang, R. P.-L.; Wong, K. M.-C.; Cheung, K.-K. *Organometallics* **2001**, *20*, 4476.

(39) (a) Sun, W.; Li, Y.; Pritchett, T. M.; Ji, Z.; Haley, J. E. *Nonlinear Opt., Quantum Opt.* **2010**, *40*, 163. (b) Li, Y.; Pritchett, T. M.; Shao, P.; Haley, J. E.; Zhu, H.; Sun, W. *J. Organomet. Chem.* **2009**, *694*, 3688. (c) Li, Y.; Pritchett, T. M.; Huang, J.; Ke, M.; Shao, P.; Sun, W. *J. Phys. Chem. A* **2008**, *112*, 7200. (d) Si, J.; Yang, M.; Wang, Y.; Zhang, L.; Li, C.; Wang, D.; Dong, S.; Sun, W. *Appl. Phys. Lett.* **1994**, *64*, 3083. (e) McKay, T. J.; Staromlynska, J.; Davy, J. R.; Bolger, J. A. *J. Opt. Soc. Am. B* **2001**, *18*, 358. (f) Song, Y.; Fang, G.; Wang, Y.; Liu, S.; Li, C.; Song, L.; Zhu, Y.; Hu, Q. *Appl. Phys. Lett.* **1999**, *74*, 332. (g) Pittman, M.; Plaza, P.; Martin, M. M.; Meyer, Y. H. *Opt. Commun.* **1998**, *158*, 201. (h) Perry, J. W.; Mansour, K.; Lee, I. Y. S.; Wu, X. L.; Bedworth, P. V.; Chen, C. T.; Ng, D.; Marder, S. R.; Miles, P.; Wada, T.; Tian, M.; Sasabe, H. *Science* **1996**, *273*, 1533. (i) Guha, S.; Kang, K.; Porter, P.; Roach, J. E.; Remy, D. E.; Aranda, F. J.; Rao, D. V. G. L. N. *Opt. Lett.* **1992**, *17*, 264. (j) Westlund, R.; Glimsdal, E.; Lindgren, M.;

Vestberg, R.; Hawker, C.; Lopez, C.; Malmström, E. *J. Mater. Chem.* **2008**, *18*, 166. (k) Glimsdal, E.; Carlsson, M.; Eliasson, B.; Minaev, B.; Lindgren, M. *J. Phys. Chem. A* **2007**, *111*, 244.